Biomechanics and Modeling in Mechanobiology (2024) 23:1179–1196
https://doi.org/10.1007/s10237-024-01832-8

ORIGINAL PAPER

A mechanics theory for the exploration of a high-throughput, sterile 3D in vitro traumatic brain injury model

Yang Wan[1] · Rafael D. González-Cruz[2,3] · Diane Hoffman-Kim[2,3,4] · Haneesh Kesari[1]

Received: 29 August 2023 / Accepted: 19 February 2024 / Published online: 6 July 2024

Abstract

Brain injuries resulting from mechanical trauma represent an ongoing global public health issue. Several in vitro and in vivo models for traumatic brain injury (TBI) continue to be developed for delineating the various complex pathophysiological processes involved in its onset and progression. Developing an in vitro TBI model that is based on cortical spheroids is especially of great interest currently because they can replicate key aspects of in vivo brain tissue, including its electrophysiology, physicochemical microenvironment, and extracellular matrix composition. Being able to mechanically deform the spheroids are a key requirement in any effective in vitro TBI model. The spheroids' shape and size, however, make mechanically loading them, especially in a high-throughput, sterile, and reproducible manner, quite challenging. To address this challenge, we present an idea for a spheroid-based, in vitro TBI model in which the spheroids are mechanically loaded by being spun by a centrifuge. (An experimental demonstration of this new idea will be published shortly elsewhere.) An issue that can limit its utility and scope is that imaging techniques used in 2D and 3D in vitro TBI models cannot be readily applied in it to determine spheroid strains. In order to address this issue, we developed a continuum mechanics-based theory to estimate the spheroids' strains when they are being spun at a constant angular velocity. The mechanics theory, while applicable here to a special case of the centrifuge-based TBI model, is also of general value since it can help with the further exploration and development of TBI models.

Keywords TBI · Brain · Trauma · Mechanobiology · Cell Mechanics · Continuum

1 Introduction

Traumatic brain injury (TBI) affects around 55 million people around the world each year and represents an ongoing global public health issue (Maas et al. 2022). Its prevalence and incidence are higher than other common neurological diseases, including stroke, Alzheimer's and Parkinson's diseases (Maas et al. 2022). In the US and Europe, 190–225 patients die every day after suffering from a TBI event and tens of thousands suffer from chronic neurodegenerative diseases and complications resulting from the injury (TBI Data 2023; Maas et al. 2022). The high mortality and long-term disability associated with TBI highlight the need for further research into its treatment and diagnosis. Currently, there are no FDA approved treatments (FDA 2021) for TBI. Traumatic brain injury is often diagnosed using a combination of standard-of-care imaging techniques such as computed tomography (CT) (Maas et al. 2005) and magnetic resonance imaging (MRI) scans (McDonald et al. 2012), as

Y. Wan and R. D. González-Cruz have contributed equally to this work.

✉ Haneesh Kesari
haneesh_kesari@brown.edu

Yang Wan
yang_wan@brown.edu

Rafael D. González-Cruz
rafael_gonzalez_cruz@brown.edu

Diane Hoffman-Kim
diane_hoffman-kim@brown.edu

[1] School of Engineering, Brown University, Providence, RI 02912, USA

[2] Department of Neuroscience, Brown University, Providence, RI 02912, USA

[3] Robert J. and Nancy D. Carney Institute for Brain Science, Brown University, Providence, RI 02906, USA

[4] Center for Biomedical Engineering, Brown University, Providence, RI 02912, USA

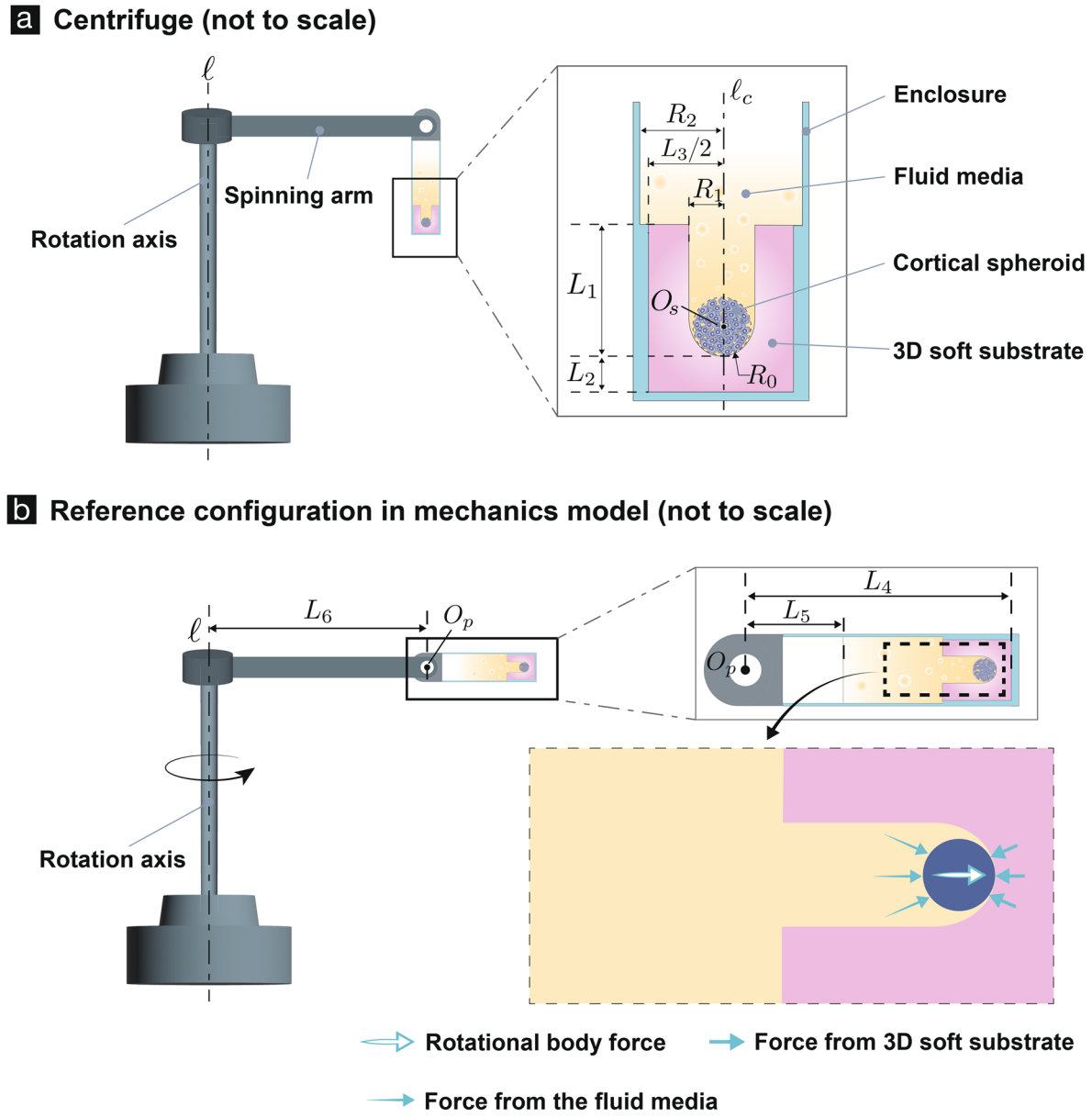
a Centrifuge (not to scale)
ℓ
Spinning arm
Rotation axis
ℓ_c
R_2
$L_3/2$
R_1
L_1
O_s
L_2
R_0
Enclosure
Fluid media
Cortical spheroid
3D soft substrate
b Reference configuration in mechanics model (not to scale)
L_6
O_p
L_4
L_5
Rotation axis
Rotational body force
Force from 3D soft substrate
Force from the fluid media
c Cortical spheroid (to scale)
Undeformed configuration
Deformed configuration
Rotational body force
Force from the fluid media
Force from 3D soft substrate

◂**Fig. 1** An illustration of the centrifuge-TBI-model. For ease of exposition, especially when we develop the mechanics theory in Sect. 4, we only show one cortical spheroid as being spun in (**a**) and (**b**). However, in practice, several thousands of spheroids can be spun simultaneously

well as neurological scales assessing consciousness like the Glasgow Coma Scale (Teasdale and Jennett 1974).

Traumatic brain injury is a disease process rather than an event (Masel and DeWitt 2010). For developing effective treatments, it is critical to understand both TBI's onset (primary injuries) and its progression (secondary injuries). As such, several in vivo as well as in vitro TBI models have been developed for delineating the various complex pathophysiological processes involved in its onset and progression. In vivo TBI studies have relied extensively on rodent models. They include injury modalities such as controlled cortical impact (CCI) (Clark et al. 1994), fluid percussion injury (FPI) (McIntosh et al. 1989), weight drop (Feeney et al. 1981) and sustained focal compression (Lin et al. 2010). As a whole, in vivo injury models are very attractive because they are all-encompassing: They include the brain's vasculature and structural organization, the brain's multiple, distinct cell types, the blood-brain barrier, and access to blood circulation and peripheral immune cells. That is, they allow the study of complex multicellular, mechanistic, and systems-level responses to TBI, including axonal demyelination, blood-brain barrier breakdown, peripheral immune cell-mediated inflammation, and neurocognitive impairment.

The in vivo injury models, however, can also have a few limitations. (1) The in vivo models' all-encompassing nature also makes them difficult to interpret. Specifically, in *in vivo* injury models, it is difficult to delineate how the various cellular, biochemical, and biophysical processes affect each other. The various processes have a complex interdependence on each other and form feedback loops that drive the disease progression. (2) The in vivo models can be expensive, and (3) difficult to use. (4) In in vivo models, it is difficult to visualize brain tissue deformation in real time and correlate injury severity to those deformations. Such correlations can potentially provide valuable information for developing inertial-sensor-system-based diagnosis techniques for mild TBI (mTBI) (Rahaman et al. 2020; Wan et al. 2022, 2023; Carlsen et al. 2021).

In vitro TBI models in most cases circumvent the limitations (1)–(3) of the in vivo models. That is, they are easier to interpret, are less expensive, are easier to use, and pose fewer ethical concerns compared to their in vivo counterparts. The earliest in vitro studies involved subjecting neuronal and glial monolayers (2D cell cultures) to higher pressures and monitoring plasma membrane damage and cell death (Murphy and Horrrocks 1993). In fact, the 2D in vitro models do not even suffer from limitation (4) of the in vivo models, since it is straightforward to monitor deformations in them using a time sequence of microscopy images and image processing algorithms. Despite their many attractive features, 2D in vitro models suffer from one major limitation: They may not be sophisticated enough to capture the primary pathophysiological processes involved in TBI.

Three dimensional (3D) cell culture models are a relatively recent development (Hanna and Pfister 2023). They are generally more sophisticated than 2D cell culture models. In particular, cortical spheroids—which are a special type of 3D cell culture model—replicate key aspects of in vivo brain tissue, such as the electrophysiology, dimensionality, physicochemical microenvironment, and the extracellular matrix composition observed (Dingle et al. 2015; Shoemaker et al. 2021) in vivo. Hence, currently there is significant interest in developing in vitro TBI models that are based on 3D cell culture models. Some recent works in this direction involve compressing neuronal cells embedded in hydrogels made of specific extracelullar matrix proteins or biomaterial composites (Bar-Kochba et al. 2016; Liaudanskaya et al. 2020), and brain organoids (Shoemaker et al. 2021). The two main challenges in developing 3D in vitro TBI models are (1) designing a mechanical loading system that can be used to mimic the mechanical forces that in vivo tissue experiences during TBI while maintaining high throughput, and sterility in the experiment, and (2) being able to estimate the deformations experienced by the in vitro tissue during the experiment.

We propose a new 3D in vitro TBI model in which mechanical loads are applied to cortical spheroids, via the aid of centrifugal forces. Cortical spheroids are grown within a 3D soft substrate, i.e., within the cavities (such as microwells) molded into the surface of a soft material (see inset in Fig. 1a), such as an agarose hydrogel. Cell culture media bathes the cortical spheroids as well as their soft substrate. We propose to load the cortical spheroids by spinning them along with their soft substrates and their fluid media using a centrifuge (see Fig. 1a). The centrifuge's angular velocity can vary during the experiment. In a frame that rotates with the centrifuge's rotating arm, the cortical spheroid, the soft substrate, and the fluid media experience body forces that push them away from the axis of rotation (Fig. 1b). These forces cause the fluid media and the soft substrate to push the cortical spheroid's surfaces that they are, respectively, in contact with toward each other, thus squeezing the spheroid (Fig. 1c). We will experimentally demonstrate in a follow-up publication that this centrifugation-based method of loading the cortical spheroids can provide the basis for the development of a high throughput and sterile in vitro 3D TBI model.

The above proposed centrifugation-based 3D in vitro TBI model (centrifuge-TBI-model) does not have the limitations (1)–(3) of the in vivo models, neither does it have the limitation of insufficient sophistication of the 2D in vitro models. The model is designed to be high throughput; maintain

conditions that are as sterile as those present at the time the spheroids are grown; and allow loading of the spheroids in a reproducible manner.

The centrifuge-TBI-model is of high throughput, since thousands of spheroids can be grown simultaneously, and then spun simultaneously as well[1]; with no steps between the two that involve processing the spheroids serially, such as individual pipetting, positioning, or probing. These features are possible for the following reasons. The 3D soft substrate is micromachined to have close to a hundred cavities/microwells on it. A single spheroid (which could be as large as 8000 cells) grows in a cavity via self-assembly given the nonadhesive properties of the soft substrate. It has already been demonstrated that using the 3D soft substrates several thousands of spheroids can be grown simultaneously (Dingle et al. 2015). A single substrate is usually smaller than a cubic centimeter in size; therefore, a lab grade centrifuge will be able to hold over a hundred substrates. Hence, several thousands of spheroids can be spun simultaneously if desired. In addition to the growth and loading operations in the centrifuge-TBI-model each being parallel in nature, another aspect of the model that critically contributes to it being high throughput is that the spheroids are loaded in situ, i.e., they are tested in the same substrate as that in which they are grown (compare, e.g., Fig. 1a and b).

The loading conditions are sterile due to the in situ testing and because the loading on the spheroids is being primarily performed by the same fluid media and the soft substrate used to grow them (e.g., see Figs. 1c and d).

The mechanical loading, i.e., the force on the spheroids, in the experiment can be easily and robustly tuned via the centrifuge's angular velocity and the volume of the fluid media.

However, as with all models, the proposed model too has some limitations. One of the most significant of those is the same as limitation (4) of the in vivo models, which, to reiterate, is the inability to visualize tissue deformation in real time and correlate injury severity to those deformations. In order to address this limitation, in this paper, we consider a special case of the centrifuge-TBI-model and develop a mechanics theory for determining the cortical spheroids' deformation in it. The special case we consider is the one which the centrifuge's angular velocity is constant as a function of time. The primary assumptions in our mechanics theory are described in Sect. 2. The mathematical preliminaries necessary for detailing our theory are described in Sect. 3. We develop the theory in Sect. 4 and summarize it in Sect. 5. Results from numerical solutions of our theory for two representative values of centrifuge angular velocity are presented in Sect. 6.

The proposed centrifuge-TBI-model, in theory, has many advantages compared to other models. The theory developed in this paper applies to a special case of the centrifuge-TBI-model, and it provides an indirect means of determining the deformations. Future studies will work toward a general and direct approach for determining deformations. We believe that our theory is of value since it allows us to explore the centrifuge-TBI-model and its viability and potential for in vitro TBI studies.

2 Primary assumptions and modeling decisions and their underlying rationale

In this section, we list some of the primary assumptions and modeling decisions that we made for developing our theory to estimate the deformations in the cortical spheroid as it is spun by the centrifuge.

As we already mentioned in Sect. 1, we restrict ourselves to the case where the centrifuge is being operated at a constant angular velocity of $\omega_{\max}$ rad/s. We made this decision in order to reduce the theory's complexity.

For modeling the deformations of the cortical spheroid, we also model the motion and deformations of the 3D soft substrate containing it, and the fluid media that bathes the spheroid and the substrate.

We ignore acceleration due to gravity in our theory.[2]

We assume that the deformations and stresses in the spheroid and the substrate's region that is in its vicinity are axi-symmetric.

We assume that the mechanics of the spheroid, the substrate, and the fluid media can be well modeled using continuum theories (Gurtin 1982). Consequently, we model the spheroid and the substrate as homogeneous solids and the fluid media as a homogeneous fluid. Even more specifically, we model the spheroid as a spherical ball composed of an incompressible neo-Hookean material, the substrate as composed of a compressible neo-Hookean material, and the fluid media as an incompressible Newtonian fluid. The constitutive law for the fluid media is given in Sect. 4.3 and those for the spheroid and substrate are given in Sect. 4.4. Additionally, we model the interaction between the spheroid and substrate as non-adhesive frictionless contact. We refer to *(i)* the cortical spheroid, *(ii)* the 3D soft substrate, and *(iii)* the fluid media collectively as the continua.

[1] In Fig. 1, we only show a single cortical spheroid being spun, even though in practice, several thousand can be spun simultaneously. We do so since showing a single spheroid makes it easier to use Fig. 1 to explain the development of the mechanics theory.

[2] This assumption is only valid when the centrifuge's angular velocities and the spheroid's distance from the centrifuge rotation axis at those velocities are such that the centripetal accelerations in and around the vicinity of the spheroid are much larger than the acceleration due to gravity. We assume that this in fact is always the case in the centrifuge-mTBI-model, which our theory is intended to model.

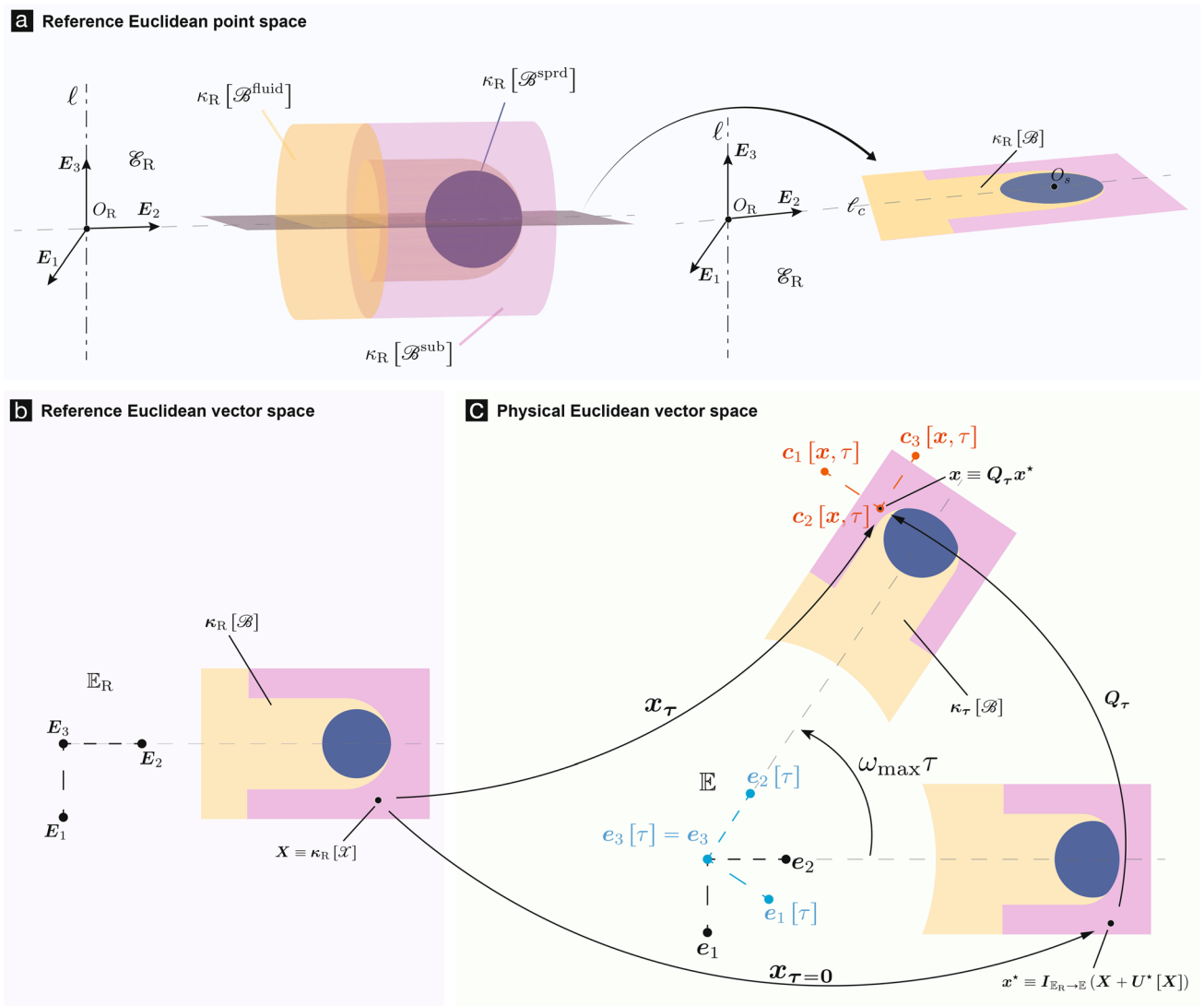

Fig. 2 An illustration of the various mathematical objects that we use in our mechanics model of spheroid centrifugation. All objects are defined in Sects. 3 and 4.1. In (c) the point marked $c_i\,[x,\tau]$, $i \in \{1, 2, 3\}$, is a vector obtained by translating $c_i\,[x,\tau]$ with x. We show the translated version instead of the original one for clarity.

We assume that in a frame that rotates with the centrifuge's spinning arm, all mechanical fields remain stationary w.r.t. time. (see Sect. 7 for a discussion of this important assumption).

On account of the previous assumption, it follows that the motion of the continua can be described as

$$\boldsymbol{x}_{\boldsymbol{\tau}}[\boldsymbol{X}] = \boldsymbol{Q}_{\boldsymbol{\tau}}\boldsymbol{I}_{\mathbb{E}_{\mathrm{R}}\to\mathbb{E}}\big(\boldsymbol{X} + \boldsymbol{U}^{\star}[\boldsymbol{X}]\big). \tag{1}$$

Here, $\boldsymbol{X}$ is the position vector of a continuum material particle $\mathscr{X}$ in a reference configuration (The particle can belong to the spheroid, the soft substrate, or the fluid media). We will henceforth be referring to the material particle $\mathscr{X}$ by its reference position vector, $\boldsymbol{X}$. We call $\boldsymbol{x}_{\boldsymbol{\tau}}[\cdot]$ the deformation map and $\boldsymbol{x}_{\boldsymbol{\tau}}[\boldsymbol{X}]$ the material particle $\boldsymbol{X}$'s current position vector at the time instance $\boldsymbol{\tau}$. We call $\boldsymbol{U}^{\star}[\boldsymbol{X}]$, the intermediate displacements of the material particle $\boldsymbol{X}$. In general, the intermediate displacements in addition to $\boldsymbol{X}$ also depend on the time instance $\boldsymbol{\tau}$. In our theory, the intermediate displacements only depending on $\boldsymbol{X}$ too are a consequence of our previous assumption. We define the symbols $\boldsymbol{Q}_{\boldsymbol{\tau}}$, and $\boldsymbol{I}_{\mathbb{E}_{\mathrm{R}}\to\mathbb{E}}$ appearing in (1) in Sect. 4.1.2. For a mathematically complete and rigorous formulation of (1) see (Wan et al. 2023).

The material field $\boldsymbol{U}^{\star}[\cdot]$ is an unknown *a priori*. The strains and the stresses in the continua depend on the values of its gradient, $\{\boldsymbol{\nabla}_{\boldsymbol{X}}[\boldsymbol{U}^{\star}]\}[\cdot]$. In Sect. 4, we derive the equations whose solution (cf. Sects. 5 and 6) will yield $\boldsymbol{U}^{\star}[\cdot]$ and hence, the strains and the stresses.

3 Mathematical preliminaries

In this section, we present the preliminary mechanics and mathematical notions that are needed for the development of our theory. Some of these notions can also be found in (Wan et al. 2022, Sect. 2.1) and (Rahaman et al. 2020, Sect. 2.1).

3.1 Abstract vector spaces in our model

Let $\mathbb{E}_{\mathrm{R}}$ be an oriented Euclidean vector space, i.e., an oriented finite dimensional, real, inner product space, and let the affine point space $\mathscr{E}_{\mathrm{R}}$ have $\mathbb{E}_{\mathrm{R}}$ as its associated vector translation space. We refer to $\mathbb{E}_{\mathrm{R}}$ and $\mathscr{E}_{\mathrm{R}}$ as the reference Euclidean vector and point space, respectively. Let $\mathbb{E}$ and $\mathscr{E}$ be another pair of Euclidean vector and affine point space, respectively. Our continua (which can either be the spheroid, the 3D soft substrate, or the fluid media) execute their motion in $\mathscr{E}$. For that reason, we refer to $\mathbb{E}$ and $\mathscr{E}$ as the physical Euclidean vector space and point space, respectively. We model each of our continuum bodies, spheroid, soft substrate, and the media using the topological spaces $\mathscr{B}^{\mathrm{sprd}}$, $\mathscr{B}^{\mathrm{sub}}$, and $\mathscr{B}^{\mathrm{fluid}}$, respectively (see Fig. 2a).

We call a select continuous, injective map from $\mathscr{B}$ (which can be $\mathscr{B}^{\mathrm{fluid}}$, $\mathscr{B}^{\mathrm{sprd}}$, or $\mathscr{B}^{\mathrm{sub}}$) into $\mathbb{E}_{\mathrm{R}}$ the reference configuration and denoted it as $\boldsymbol{\kappa}_{\mathrm{R}}$. The elements of $\mathscr{B}$ are called material particles. We call $\boldsymbol{X} \equiv \boldsymbol{\kappa}_{\mathrm{R}}[\mathscr{X}]$ the particle $\mathscr{X}$'s reference position vector and $\boldsymbol{\kappa}_{\mathrm{R}}[\mathscr{B}]$ the reference body (see Fig. 2b). Taking some arbitrary point $O_{\mathrm{R}} \in \mathscr{E}_{\mathrm{R}}$ to be $\mathscr{E}_{\mathrm{R}}$'s origin (see Fig. 2a), to $\boldsymbol{\kappa}_{\mathrm{R}}$ we associate the map $\kappa_{\mathrm{R}} : \mathscr{B} \to \mathscr{E}_{\mathrm{R}}$ such that $O_{\mathrm{R}} + \boldsymbol{\kappa}_{\mathrm{R}}[\mathscr{X}] = \kappa_{\mathrm{R}}[\mathscr{X}]$. We call $X \equiv \kappa_{\mathrm{R}}[\mathscr{X}]$ the particle $\mathscr{X}$'s reference point.

We model time as a one-dimensional normed vector space $\mathbb{T}$ and denote a typical element in it as $\boldsymbol{\tau} = \tau \boldsymbol{s}$, where $\tau \in \mathbb{R}$ and $\boldsymbol{s}$ is a fixed vector which has units of seconds.

3.2 Cartesian basis vectors

The sets $\left(\boldsymbol{E}_i\right)_{i\in\mathscr{I}}$ and $\left(\boldsymbol{e}_i\right)_{i\in\mathscr{I}}$, where $\mathscr{I} := (1,2,3)$, are orthonormal sets of basis vectors for $\mathbb{E}_{\mathrm{R}}$ and $\mathbb{E}$, respectively. By orthonormal, we mean that the inner product between $\boldsymbol{E}_i$ and $\boldsymbol{E}_j$, or $\boldsymbol{e}_i$ and $\boldsymbol{e}_j$, where $i, j \in \mathscr{I}$, equals δ_{ij}, the Kronecker delta symbol, which equals unity iff $i = j$ and zero otherwise. In our problem, we take $\boldsymbol{E}_i$ and $\boldsymbol{e}_i$, $i \in \mathscr{I}$, to have the units of meters. The Cartesian co-ordinates of X which we denote as $\check{\mathbf{X}}[X] = \left(\check{\mathbf{X}}_i[X]\right)_{i\in\mathscr{I}}$ are components of $\boldsymbol{X}$ w.r.t. $\boldsymbol{E}_i$, that is $\check{\mathbf{X}}_i[X] = X_i$, where $X_i := \boldsymbol{X} \cdot \boldsymbol{E}_i$. For simplicity, $\mathbf{X} \equiv \left(X_1, X_2, X_3\right)$.

We denote the space of all $m \times n$ real nested ordered sets, where $m, n \in \mathbb{N}$, as $\mathscr{M}_{m\times n}(\mathbb{R})$. Thus, $\check{\mathbf{X}}[X] \in \mathscr{M}_{3\times 1}(\mathbb{R})$. We call the map $\mathscr{E}_{\mathrm{R}} \ni X \mapsto \check{\mathbf{X}}[X] \in \mathscr{M}_{3\times 1}(\mathbb{R})$ the Cartesian co-ordinate map. Let $\left(\mathbf{x}_i\right)_{i\in\mathscr{I}}$ be an orthonormal set of basis vectors for $\mathscr{M}_{3\times 1}(\mathbb{R})$, or $\mathbb{R}^3$, where $\mathbf{x}_1 := (1,0,0)$, $\mathbf{x}_2 := (0,1,0)$, and $\mathbf{x}_3 := (0,0,1)$. When we refer to $\boldsymbol{X} \in \mathbb{E}_{\mathrm{R}}$, $\mathbf{X} \in \mathscr{M}_{3\times 1}(\mathbb{R})$, or $X \in \mathscr{E}_{\mathrm{R}}$ as a material particle we in fact mean the material particle $\mathscr{X} \in \mathscr{B}$.

3.3 Co-rotational Cartesian basis vectors for $\mathbb{E}$

Let

$$\left(Q_{ij}[\tau]\right)_{i,j\in\mathscr{I}} = \begin{pmatrix} \cos\left[\omega_{\max}\tau\right] & -\sin\left[\omega_{\max}\tau\right] & 0 \\ \sin\left[\omega_{\max}\tau\right] & \cos\left[\omega_{\max}\tau\right] & 0 \\ 0 & 0 & 1 \end{pmatrix} :=: \mathbf{Q}[\tau]. \tag{2}$$

The matrix $\mathbf{Q}[\tau]$ belongs to the special orthonormal group $SO(3) \subset \mathscr{M}_{3\times 3}(\mathbb{R})$ and therefore, satisfies the equations

$$\mathbf{Q}^{\mathsf{T}}[\tau]\,\mathbf{Q}[\tau] = \mathbf{I}_{3\times 3}, \tag{3a}$$

and

$$\mathbf{Q}[\tau]\,\mathbf{Q}^{\mathsf{T}}[\tau] = \mathbf{I}_{3\times 3}, \tag{3b}$$

where $\mathbf{Q}^{\mathsf{T}}[\tau]$ is the transpose of $\mathbf{Q}[\tau]$, i.e., $\mathbf{Q}^{\mathsf{T}}[\tau] = (\mathbf{Q}[\tau])^{\mathsf{T}}$, and $\mathbf{I}_{3\times 3} = \left(\delta_{ij}\right)_{i,j\in\mathscr{I}} \in \mathscr{M}_{3\times 3}(\mathbb{R})$.

Using $\mathbf{Q}[\tau]$ we define the co-rotational set of basis vectors for $\mathbb{E}$, $(\boldsymbol{e}_i[\tau])_{i\in\mathscr{I}}$, as

$$\boldsymbol{e}_i[\tau] = Q_{ji}[\tau]\boldsymbol{e}_j. \tag{4}$$

Note that $(\boldsymbol{e}_i[\tau])_{i\in\mathscr{I}}$ change with time (see Fig. 2c). However, at each time instance $\boldsymbol{\tau}$, they form an orthonormal set of vectors and provide a basis for $\mathbb{E}$.

3.4 Co-rotational Cartesian co-ordinates

Given $\boldsymbol{x} \in \mathbb{E}$, let

$$\check{x}_i[\boldsymbol{x}, \tau] := \boldsymbol{x} \cdot \boldsymbol{e}_i[\tau], \tag{5}$$

where $(\boldsymbol{e}_i[\tau])_{i\in\mathscr{I}}$ is defined via (4). We call $(\check{x}_i[\boldsymbol{x},\tau])_{i\in\mathscr{I}} =: \check{\mathbf{x}}[\boldsymbol{x},\tau]$ the co-rotational Cartesian co-ordinates of $\boldsymbol{x}$ at the time instance τ.

3.5 Co-rotational cylindrical basis vectors for $\mathbb{E}$

Using $\check{\mathbf{x}}[\boldsymbol{x},\tau]$, we define the set of co-rotational cylindrical basis vectors $\left(\boldsymbol{c}_i[\boldsymbol{x},\tau]\right)_{i\in\mathscr{I}}$ (see Fig. 2c) at the point $\boldsymbol{x}$ at the time instance τ as

$$\left(\boldsymbol{c}_i[\boldsymbol{x},\tau]\right)_{i\in\mathscr{I}} = \mathbf{R}\left[\check{\mathbf{x}}[\boldsymbol{x},\tau]\right]\left(\boldsymbol{e}_i[\tau]\right)_{i\in\mathscr{I}}, \tag{6}$$

where $\mathbf{R}[\cdot] : \mathscr{M}_{3\times 1}(\mathbb{R}) \to \mathscr{M}_{3\times 3}(\mathbb{R})$,

Table 1 Typical values for the geometry parameters R_0–R_2, and L_1–L_6 in the centrifuge-TBI-model

Parameter name	R_0	R_1	R_2	L_1	L_2	L_3	L_4	L_5	L_6
Parameter value $\times 10^3$	0.08	0.2	7.96	0.8	1.5	0.8	66	59.61	112.69

These parameters are defined in Fig. 1a and b. These typical values are based on the spheroid, and 3D soft substrate dimensions reported in (Dingle et al. 2015); geometry of the enclosure (marked in Fig. 1a) in which the 3D soft substrate containing the spheroid is typically held; the amount of fluid media that is typically added to the enclosure, which is around 1 ml (Dingle et al. 2015); and the dimensions of a typical lab grade centrifuge, such as 5810R Eppendorf https://www.eppendorf.com/us-en. The units of all parameters are *meters*

$$\mathbf{R}\big[(x_1,x_2,x_3)\big] := \frac{1}{\sqrt{x_1^2+x_3^2}}\begin{pmatrix} x_1 & 0 & x_3 \\ x_3 & 0 & -x_1 \\ 0 & \sqrt{x_1^2+x_3^2} & 0 \end{pmatrix}. \tag{7}$$

3.6 Linear maps between vector spaces

Say $\mathbb{W}$ and $\mathbb{U}$ are two arbitrary, oriented Euclidean vector spaces; for instance, they can be $\mathbb{E}_{\mathrm{R}}$ and $\mathbb{E}$. We denote the space of all linear maps (transformations/operators) from $\mathbb{W}$ to $\mathbb{U}$ as $\mathscr{L}(\mathbb{W},\mathbb{U})$. We denote the norm of a vector $\boldsymbol{w}_1$ in $\mathbb{W}$ that is induced by $\mathbb{W}$'s inner product, i.e., $(\boldsymbol{w}_1\cdot\boldsymbol{w}_1)^{1/2}$, as $\|\boldsymbol{w}_1\|$. For $\boldsymbol{u}_1\in\mathbb{U}$, the expression $\boldsymbol{u}_1\otimes\boldsymbol{w}_1$ denotes the linear map from $\mathbb{W}$ to $\mathbb{U}$ defined as

$$\big(\boldsymbol{u}_1\otimes\boldsymbol{w}_1\big)\boldsymbol{w}_2 = \boldsymbol{u}_1\big(\boldsymbol{w}_1\cdot\boldsymbol{w}_2\big), \tag{8}$$

where $\boldsymbol{w}_2\in\mathbb{W}$. If the sets $\big(\boldsymbol{u}_i\big)_{i\in\mathscr{I}}$ and $\big(\boldsymbol{w}_i\big)_{i\in\mathscr{I}}$ provide bases for $\mathbb{U}$ and $\mathbb{W}$, respectively, then, it can be shown that $\Big(\big(\boldsymbol{u}_i\otimes\boldsymbol{w}_j\big)_{j\in\mathscr{I}}\Big)_{i\in\mathscr{I}}$, which we will henceforth abbreviate as $\big(\boldsymbol{u}_i\otimes\boldsymbol{w}_j\big)_{i,j\in\mathscr{I}}$, provides a basis for $\mathscr{L}(\mathbb{W},\mathbb{U})$. The number T_{ij}, where $i,j\in\mathscr{I}$, is called the component of $\boldsymbol{T}\in\mathscr{L}(\mathbb{W},\mathbb{U})$ w.r.t. $\boldsymbol{u}_i\otimes\boldsymbol{w}_j$ iff $T_{ij}=\boldsymbol{u}_i\cdot\big(\boldsymbol{T}\boldsymbol{w}_j\big)$. We call the nested ordered set $\big(T_{ij}\big)_{i,j\in\mathscr{I}}$ the component form of $\boldsymbol{T}$ w.r.t. $\big(\boldsymbol{u}_i\otimes\boldsymbol{w}_j\big)_{i,j\in\mathscr{I}}$ and denote it as $\mathbf{T}$.

From here on, unless otherwise specified, we will be following the Einstein summation convention. As per this convention, a repeated index in a term will imply a sum over that term with the repeated index taking values in $\mathscr{I}$. For example, the expression $X_i\boldsymbol{E}_i$ represents the sum $\sum_{i\in\mathscr{I}}X_i\boldsymbol{E}_i$. And an unrepeated index in a term will signify a set of 3 terms. For example, the term $\boldsymbol{E}_i$ represents the set $\big\{\boldsymbol{E}_i\,\big|\,i\in\mathscr{I}\big\}$.

The operator $D_j[\cdot]$ is defined such that

$$\big\{D_j\big[f\big]\big\}[\mathbf{X}] = \frac{\partial f[\mathbf{X}]}{\partial X_j}, \tag{9}$$

for $f:\mathbb{R}^3\to\mathbb{R}$. We abbreviate $D_j\big[f\big]$ as D_jf.

4 Mechanics Model

4.1 Kinematics

4.1.1 Stationary and reference configurations

We show our assumed geometries for the continua in the centrifuge-TBI-model in Fig. 1a and b. The configuration shown in (a) is for when the centrifuge is stationary (recall that we have ignored acceleration due to gravity), and the one shown in (b) is the reference configuration in our problem.

In Fig. 1a, the spheroid lies in a 3D soft substrate, while the 3D soft substrate itself lies in an enclosure connected to the centrifuge's spinning arm. The geometries of the spheroid, the substrate, and the enclosure are all axi-symmetric about the axis ℓ_c shown in Fig. 1a. Thus, the spheroid is, well, a spherical ball of radius R_0 m. The cavity in the substrate that the spheroid lies in has the shape of a test tube. It is open at the top; it is L_1 m deep; the radius of its circular cross-sections is R_1 m; and its base has a hemispherical shape. The substrate does not completely fill the enclosure. The substrate's cross-sections toward the top are annular disks, while those toward the bottom are circular disks. The inner radii of the annular disks are R_1 m. The outer radii of the annular disks (and the radii of the circular disks) is $L_3/2$ m. The enclosure's cross-sections toward the top as well as those toward the bottom are both annular disks, albeit of different inner radii. The inner radii of the enclosure's annular disks that lie toward the bottom are the same as the outer radii of the substrate's annular disks, namely $L_3/2$ m. The inner radii of the enclosure's annular disks that lie toward the top are R_2 m.

The spheroid's center O_s lies on the central axis ℓ_c (see Fig. 1a), and it rests at the bottom of the cavity, with a single point touching (see Fig. 1a). The thickness of the substrate under the spheroid is L_2 m.

We refer to the point at which the centrifuge's spinning arm attaches to the enclosure as O_P (marked in Fig. 1b). We take the reference configuration for our problem to be the one shown in Fig. 1b, which is the same as that in Fig. 1a except that the enclosure and the continua have undergone a rigid body rotation about the axis that is perpendicular to the

plane spanned by the centrifuge's rotation axis and spinning arm (shown in Fig. 1a) and passing through O_P.[3]

The base of the substrate is at a distance of L_4 m from the point O_P (shown in Fig. 1b). The spheroid and the substrate are bathed in the fluid media. The surface of the fluid media is at a distance of L_5 m from the point O_P (shown in Fig. 1b). The length of the spinning arm is L_6 m.

Typical values for all the geometry parameters in the stationary and reference configurations, which are partially based on the measurements reported in (Dingle et al. 2015), are given in Table 1.

4.1.2 Deformation mapping

The motion of the continua is given by (1). To partially reiterate, the vector $\boldsymbol{X} \in \mathbb{E}_{\mathrm{R}}$ is the reference position vector of the material particle $\mathscr{X}$. The symbol $\boldsymbol{I}_{\mathbb{E}_{\mathrm{R}} \to \mathbb{E}}$ denotes the identity linear map from $\mathbb{E}_{\mathrm{R}}$ onto $\mathbb{E}$. More explicitly, $\boldsymbol{I}_{\mathbb{E}_{\mathrm{R}} \to \mathbb{E}} = \boldsymbol{e}_i \otimes \boldsymbol{E}_i$. Without loss of generality, we take that the continua rotate about $\boldsymbol{e}_3$. Since we restrict ourselves to the case in which the continua rotate at a fixed angular velocity of $\omega_{\max}$ rad/s, the assumption of rotation about $\boldsymbol{e}_3$ implies that $\boldsymbol{Q}_{\boldsymbol{\tau}} = Q_{ij}[\tau]\boldsymbol{e}_i \otimes \boldsymbol{e}_j$, where $Q_{ij}[\tau]$ is defined in (2). The map $\boldsymbol{U}^{\star} : \mathbb{E}_{\mathrm{R}} \to \mathbb{E}_{\mathrm{R}}$ is the intermediate displacement field of $\mathscr{B}$. The symbol $\boldsymbol{x}_{\boldsymbol{\tau}}[\boldsymbol{X}]$ is the material particle $\boldsymbol{X}$'s position vector in $\mathbb{E}$ at the time instance $\boldsymbol{\tau}$. The set $\boldsymbol{\kappa}_{\boldsymbol{\tau}}[\mathscr{B}] = \left\{\boldsymbol{x}_{\boldsymbol{\tau}}[\boldsymbol{X}] \in \mathbb{E} \,\middle|\, \boldsymbol{X} \in \boldsymbol{\kappa}_{\mathrm{R}}[\mathscr{B}]\right\}$ is called the current body (see Fig. 2c).

As per (1), the continua's deformations are time invariant in the co-rotational basis $(\boldsymbol{e}_i[\tau])_{i\in\mathscr{I}}$. The co-rotational basis themselves rotate about the time stationary vector $\boldsymbol{e}_3$ with the constant angular velocity $\omega_{\max}$ rad/s (see Fig. 2c).

4.1.3 Displacements components

Expressing $\boldsymbol{X} = X_i\boldsymbol{E}_i$, and $\boldsymbol{U}^{\star}[\boldsymbol{X}] = U_i^{\star}[\mathbf{X}]\boldsymbol{E}_i$, and using (1) and (4), it can be shown that

$$\boldsymbol{x}_{\tau}[\boldsymbol{X}] = \bar{x}_i[\mathbf{X}]\boldsymbol{e}_i[\tau], \tag{10a}$$

where

$$\bar{x}_i[\mathbf{X}] = X_i + U_i^{\star}[\mathbf{X}]. \tag{10b}$$

Denoting $(\bar{x}_i[\mathbf{X}])_{i\in\mathscr{I}}$ as $\bar{\mathbf{x}}[\mathbf{X}]$ and $\left(U_i^{\star}[\mathbf{X}]\right)_{i\in\mathscr{I}}$ as $\mathbf{U}^{\star}[\mathbf{X}]$, (10b) can equivalently be expressed as

$$\bar{\mathbf{x}}[\mathbf{X}] = \mathbf{X} + \mathbf{U}^{\star}[\mathbf{X}]. \tag{11}$$

Let

$$\boldsymbol{\kappa}_{\mathrm{R}}\left[\mathscr{B}^{\mathrm{sprd}}\right] := \left\{\mathbf{X} \in \mathbb{R}^3 \mid X_i\boldsymbol{E}_i \in \boldsymbol{\kappa}_{\mathrm{R}}\left[\mathscr{B}^{\mathrm{sprd}}\right]\right\}, \tag{12}$$

and

$$\boldsymbol{\kappa}_{\mathrm{R}}\left[\mathscr{B}^{\mathrm{sub}}\right] := \left\{\mathbf{X} \in \mathbb{R}^3 \mid X_i\boldsymbol{E}_i \in \boldsymbol{\kappa}_{\mathrm{R}}\left[\mathscr{B}^{\mathrm{sub}}\right]\right\}. \tag{13}$$

We refer to the restriction of $\bar{\mathbf{x}}[\cdot]$ to $\boldsymbol{\kappa}_{\mathrm{R}}\left[\mathscr{B}^{\mathrm{sprd}}\right]$ as $\bar{\mathbf{x}}^{\mathrm{sprd}}[\cdot]$. The maps $\bar{\mathbf{x}}^{\mathrm{sub}}[\cdot]$ and $\bar{\mathbf{x}}^{\mathrm{fluid}}[\cdot]$ are defined similarly.

4.1.4 Velocity components

We call $\mathscr{L}(\mathbb{T}, \mathbb{E})$ the physical velocity vector space and denote it as $\mathbb{V}$. It can be shown that the set $\left(\boldsymbol{v}_i[\tau]\right)_{i\in\mathscr{I}}$, where $\boldsymbol{v}_i[\tau] \in \mathbb{V}$ and are defined such that $\{\boldsymbol{v}_i[\tau]\}\boldsymbol{\tau} = \tau\boldsymbol{e}_i[\tau]$, that is $\boldsymbol{v}_i[\tau] := \boldsymbol{e}_i[\tau] \otimes \boldsymbol{s}^*$, where $\boldsymbol{s}^*$ is the dual of $\boldsymbol{s}$, provides an orthonormal basis for $\mathbb{V}$. The velocity of a material particle $\boldsymbol{X}$ executing its motion in $\mathbb{E}$ lies in $\mathbb{V}$. The velocity of the material particle $\boldsymbol{X}$ at the instant $\boldsymbol{\tau}$, which we denote as $\boldsymbol{V}_{\boldsymbol{\tau}}[X]$, equals the value of the Fréchet derivative of the map $\mathbb{T} \ni \boldsymbol{\tau} \mapsto \boldsymbol{x}_{\boldsymbol{X}}[\boldsymbol{\tau}] \in \mathbb{E}$, where $\boldsymbol{x}_{\boldsymbol{X}}[\boldsymbol{\tau}] = \boldsymbol{x}_{\boldsymbol{\tau}}[\boldsymbol{X}]$, at the time instance $\boldsymbol{\tau}$. Thus, it follows from (1) that for $\tau \geq 0$

$$\boldsymbol{V}_{\boldsymbol{\tau}}[X] = V_i[\mathbf{X}]\boldsymbol{v}_i[\tau], \tag{14a}$$

where

$$V_i[\mathbf{X}] = W_{ij}\left(X_j + U_j^{\star}[\mathbf{X}]\right), \tag{14b}$$

and

$$W_{ij} = Q'_{kj}[\tau]Q_{ki}[\tau]. \tag{14c}$$

From (2) and (14c), it follows that

$$\left(W_{ij}\right)_{i,j\in\mathscr{I}} = \begin{pmatrix} 0 & -\omega_{\max} & 0 \\ \omega_{\max} & 0 & 0 \\ 0 & 0 & 0 \end{pmatrix} =: \mathbf{W}. \tag{15}$$

Denoting $(V_i[\mathbf{X}])_{i\in\mathscr{I}}$ as $\mathbf{V}[\mathbf{X}]$, (14b) can equivalently be written as

$$\mathbf{V}[\mathbf{X}] = \mathbf{W}\left(\mathbf{X} + \mathbf{U}^{\star}[\mathbf{X}]\right). \tag{16}$$

The velocity of the material particle located at $\boldsymbol{x} \in \mathbb{E}$ at the time instance $\boldsymbol{\tau}$ is defined as

$$\boldsymbol{v}_{\boldsymbol{\tau}}[\boldsymbol{x}] = \boldsymbol{V}_{\boldsymbol{\tau}}\left[\boldsymbol{x}_{\boldsymbol{\tau}}^{-1}[\boldsymbol{x}]\right]. \tag{17}$$

From (14a), (14b), and (10b), the equation (17) can be written as

$$\boldsymbol{v}_{\boldsymbol{\tau}}[\boldsymbol{x}] = W_{ij}\check{x}_j[\boldsymbol{x}, \tau]\boldsymbol{v}_i[\tau]. \tag{18}$$

[3] Note that in our problem, the reference configuration and the configuration when the centrifuge is not spinning are not isomorphic. When the centrifuge is not spinning, the central axis and the rotation axis are parallel to each other, where as in the reference configuration, the central axis ℓ_c and the rotation axis are perpendicular to each other.

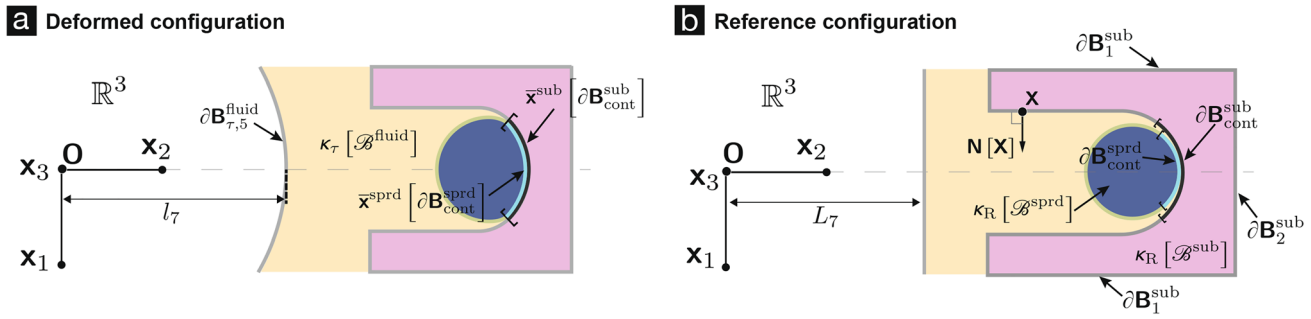

Fig. 3 An illustration of the cortical spheroid, the fluid media, and the soft substrate surfaces in the deformed (**a**) and reference (**b**) configurations

4.1.5 Accelerations

We call $\mathscr{L}(\mathbb{T},\mathbb{V})$ the physical acceleration vector space and denote it as $\mathbb{A}$. It can be shown that the set $\left(\boldsymbol{a}_i[\tau]\right)_{i\in\mathscr{I}}$, where $\boldsymbol{a}_i[\tau]\in\mathbb{A}$ and are defined such that $\{\boldsymbol{a}_i[\tau]\}\boldsymbol{\tau}=\tau\boldsymbol{v}_i[\tau]$, i.e., $\boldsymbol{a}_i[\tau]=\boldsymbol{v}_i[\tau]\otimes\boldsymbol{s}^*$, provides an orthonormal basis for $\mathbb{A}$. The acceleration of a material particle $\boldsymbol{X}$ executing its motion in $\mathbb{E}$ lies in $\mathbb{A}$. The acceleration of $\boldsymbol{X}$ at the time instance $\boldsymbol{\tau}$ equals the value of the Fréchet derivative of the map $\mathbb{T}\ni\boldsymbol{\tau}\mapsto\boldsymbol{V}_{\boldsymbol{X}}(\boldsymbol{\tau})\in\mathbb{V}$, where $\boldsymbol{V}_{\boldsymbol{X}}(\boldsymbol{\tau})=\boldsymbol{V}_{\boldsymbol{\tau}}(\boldsymbol{X})$, at the time instance $\boldsymbol{\tau}$. Thus, it follows from (14a) that for $\tau\geq 0$

$$\boldsymbol{A}_\tau[X]=A_i[\mathbf{X}]\boldsymbol{a}_i[\tau], \tag{19a}$$

where

$$A_i[\mathbf{X}]=W_{im}W_{mp}\Big(X_p+U^\star_p[\mathbf{X}]\Big). \tag{19b}$$

Denoting $(A_i[\mathbf{X}])_{i\in\mathscr{I}}$ as $\mathbf{A}[\mathbf{X}]$, (19b) can be equivalently be written as

$$\mathbf{A}[\mathbf{X}]=\mathbf{W}^2\big(\mathbf{X}+\mathbf{U}^\star[\mathbf{X}]\big). \tag{20}$$

The acceleration of the material particle located at $\boldsymbol{x}\in\mathbb{E}$ at the time instance $\boldsymbol{\tau}$ is defined as

$$\boldsymbol{a}_\tau[x]=\boldsymbol{A}_\tau\left[\boldsymbol{x}^{-1}_\tau[x]\right]. \tag{21}$$

From (19a), (19b), and (10b), the equation (21) can be written as

$$\boldsymbol{a}_\tau[x]=W_{im}W_{mp}\,\breve{x}_p[\boldsymbol{x},\tau]\boldsymbol{a}_i[\tau]. \tag{22}$$

4.1.6 Deformation gradient and Strains

The deformation gradient corresponding to the deformation mapping $\boldsymbol{x}_\tau[\cdot]$, given in (1), is

$$\{\boldsymbol{\nabla}_X\left[\boldsymbol{x}_\tau\right]\}[X]=:\boldsymbol{F}_\tau[X]=F_{ij}[\mathbf{X}]\boldsymbol{e}_i[\tau]\otimes\boldsymbol{E}_j, \tag{23a}$$

where

$$F_{ij}[\mathbf{X}]:=\delta_{ij}+D_jU^\star_i[\mathbf{X}]. \tag{23b}$$

The right Cauchy-Green deformation tensor corresponding to the deformation gradient $F_{ij}[\mathbf{X}]\boldsymbol{e}_i[\tau]\otimes\boldsymbol{E}_j$ is

$$\boldsymbol{C}[X]=C_{ij}[\mathbf{X}]\boldsymbol{E}_i\otimes\boldsymbol{E}_j, \tag{24a}$$

where

$$C_{ij}[\mathbf{X}]=F_{mi}[\mathbf{X}]F_{mj}[\mathbf{X}]. \tag{24b}$$

We abbreviate $\left(F_{ij}[\mathbf{X}]\right)_{i,j\in\mathscr{I}}$ and $\left(C_{ij}[\mathbf{X}]\right)_{i,j\in\mathscr{I}}$ as $\mathbf{F}[\mathbf{X}]$ and $\mathbf{C}[\mathbf{X}]$, respectively.

4.2 Equilibrium

4.2.1 Cauchy-momentum equations in the reference body

It follows from the principle of balance of linear momentum and our decision to ignore acceleration due to gravity that

$$\{\,\mathrm{Div}\,\boldsymbol{F}_{\boldsymbol{\tau}}\boldsymbol{S}\}[X]=\rho_0\boldsymbol{A}_\tau[X], \tag{25}$$

where $\{\,\mathrm{Div}\,\boldsymbol{F}_{\boldsymbol{\tau}}\boldsymbol{S}\}[\cdot]$ is the divergence of the field $\boldsymbol{X}\mapsto\boldsymbol{F}_{\boldsymbol{\tau}}[X]\boldsymbol{S}[X]$. Here, $\boldsymbol{S}[X]$ is the 2nd Piola–Kirchhoff stress tensor at the material particle $\boldsymbol{X}$.

In component form (25) can be written as

$$\left\{D_j\left[F_{im}S_{mj}\right]\right\}[\mathbf{X}]=\rho_0A_i[\mathbf{X}], \tag{26}$$

where $S_{ij}[\mathbf{X}]$, $i,j\in\mathscr{I}$, are the components of $\boldsymbol{S}[X]$[4].

In (26) replacing $A_i[\mathbf{X}]$ with the RHS of (19b), we get

[4] Here, we omit providing the mathematical details of how precisely $S_{ij}[\mathbf{X}]$ and $T_{ij}[\mathbf{x}]$ are, respectively, related to $\boldsymbol{S}[X]$ and $\boldsymbol{T}_{\boldsymbol{\tau}}[\boldsymbol{x}]$. Since doing so will require notions from *exterior algebra* and *differential geometry* that need a significant amount of space to properly explain and hence, would distract from the primary focus of this paper.

$$\{D_j[F_{im}S_{mj}]\}[\mathbf{X}] = \rho_0 W_{im}W_{mp}\Big(X_p + U_p^\star[\mathbf{X}]\Big), \tag{27}$$

where ρ_0 kg/m^3 is the density of the continua.

Noting from (15) that $W_{im}W_{mp} = -\omega_{\max}^2\big(\delta_{ip} - \delta_{i3}\delta_{3p}\big)$ in (27), we get

$$\{D_j[F_{im}S_{mj}]\}[\mathbf{X}] = -\rho_0\omega_{\max}^2\big(X_i + U_i^\star[\mathbf{X}] - \delta_{i3}\big(X_3 + U_3^\star[\mathbf{X}]\big)\big). \tag{28}$$

The domain of (28) is either $\kappa_R[\mathscr{B}^{\text{sprd}}]$, or $\kappa_R[\mathscr{B}^{\text{sub}}]$, which were, respectively, defined in (12) and (13). Irrespective, of whether $\mathbf{X}$ belongs to $\kappa_R[\mathscr{B}^{\text{sprd}}]$ or $\kappa_R[\mathscr{B}^{\text{sub}}]$ the co-ordinates X_1 and X_3 are always less than $L_3/2$, where recall that $L_3/2$ is the outer radii of the substrate and is 0.4×10^{-3} in our model. The co-ordinate X_2 in the domains, however, varies between 176×10^{-3} and 179×10^{-3}. (Fig. 1 can help in understanding how we arrived at these ranges for the different co-ordinates.) Therefore, in (28), we ignore X_1, and X_3, in comparison with X_2. The intermediate displacement components $U_i^\star[\mathbf{X}]$ are unlikely to be larger than the height of the substrate, which is, roughly, 3 millimeters. Therefore, we also ignore $U_i^*[\mathbf{X}]$ in comparison with X_2 in (28). In summary, we approximate (28) as

$$\{D_j[F_{im}S_{mj}]\}[\mathbf{X}] = -\rho_0\omega_{\max}^2\delta_{i2}\delta_{2j}X_j. \tag{29}$$

4.2.2 Cauchy-momentum equations in the current body

It follows from the principle of balance of linear momentum that

$$\{\ \mathrm{Div}\,\boldsymbol{T}_{\boldsymbol{\tau}}\}[\boldsymbol{x}] = \rho_\tau[\boldsymbol{x}]\boldsymbol{a}_{\boldsymbol{\tau}}[\boldsymbol{x}], \tag{30}$$

for all $\boldsymbol{x}\in\boldsymbol{\kappa}_{\boldsymbol{\tau}}[\mathscr{B}]$, where $\{\ \mathrm{Div}\,\boldsymbol{T}_{\boldsymbol{\tau}}\}[\cdot]$ is the divergence of the field $\boldsymbol{x}\mapsto\boldsymbol{T}_{\boldsymbol{\tau}}[\boldsymbol{x}]$. Here, $\boldsymbol{T}_{\boldsymbol{\tau}}[\boldsymbol{x}]$ is the Cauchy stress tensor at the current position $\boldsymbol{x}$ at the time instance $\boldsymbol{\tau}$. And $\rho_\tau[\boldsymbol{x}] := \rho_0/\mathrm{Det}\big[\boldsymbol{F}_{\boldsymbol{\tau}}\big[\boldsymbol{x}_{\boldsymbol{\tau}}^{-1}[\boldsymbol{x}]\big]\big]$, where $\mathrm{Det}[\cdot]$ is the determinant operator.

In (30) replacing $\boldsymbol{a}_{\boldsymbol{\tau}}[\boldsymbol{x}]$ with the RHS of (22) and rewriting (30) in component form, we get

$$\{D_jT_{ij}\}[\mathbf{x}] = \overline{\rho}_\tau[\mathbf{x}]W_{im}W_{mp}x_p, \tag{31}$$

for all $\mathbf{x}\in\kappa_\tau[\mathscr{B}]$,

$$\kappa_\tau[\mathscr{B}] := \big\{\mathbf{x} := (x_1,x_2,x_3)\in\mathbb{R}^3 \mid x_i\boldsymbol{e}_i[\tau]\in\boldsymbol{\kappa}_{\boldsymbol{\tau}}[\mathscr{B}]\big\}, \tag{32}$$

and $T_{ij}[\mathbf{x}]$, $i,\ j\in\mathscr{I}$, are the components of $\boldsymbol{T}_{\boldsymbol{\tau}}[\boldsymbol{x}]$ [4]. Here, $\overline{\rho}_\tau[\cdot]$ is defined such that $\overline{\rho}_\tau[\mathbf{x}] = \rho_\tau\big[x_i\boldsymbol{e}_i[\tau]\big]$. Noting from (15) that $W_{im}W_{mp} = -\omega_{\max}^2\big(\delta_{ip} - \delta_{i3}\delta_{3p}\big)$ in (31) we get

$$\{D_jT_{ij}\}[\mathbf{x}] = -\overline{\rho}_\tau[\mathbf{x}]\omega_{\max}^2\big(x_i - \delta_{i3}x_3\big). \tag{33}$$

4.3 Pressure in the fluid media

We model the fluid media as an incompressible Newtonian fluid. It can be shown that in our problem, the rate of deformation tensor is naught (see Sect. Appendix for details). Consequently, from (Gurtin 1982, Sect. 22), we can get

$$\mathbf{T}[\mathbf{x}] = -p_s^{\text{fluid}}[\mathbf{x}]\mathbf{I}_{3\times3}, \tag{34}$$

for all $\mathbf{x}\in\kappa_\tau\big[\mathscr{B}^{\text{fluid}}\big]$,

$$\kappa_\tau\big[\mathscr{B}^{\text{fluid}}\big] := \big\{\mathbf{x}\in\mathbb{R}^3 \mid x_i\boldsymbol{e}_i[\tau]\in\boldsymbol{\kappa}_{\boldsymbol{\tau}}\big[\mathscr{B}^{\text{fluid}}\big]\big\}, \tag{35}$$

and $\mathbf{T}[\mathbf{x}] := \big(T_{ij}[\mathbf{x}]\big)_{i,j\in\mathscr{I}}$ and $p_s^{\text{fluid}}[\cdot]$ is the pressure field.

In (33) substituting $\overline{\rho}_\tau[\mathbf{x}]$ as ρ_0, since we have assumed the fluid media as being incompressible, and $\mathbf{T}[\mathbf{x}]$ as $-p_s^{\text{fluid}}[\mathbf{x}]\mathbf{I}_{3\times3}$ from (34), we get that

$$\big\{D_i\big[p_s^{\text{fluid}}\big]\big\}[\mathbf{x}] = \rho_0\omega_{\max}^2\big(x_i - \delta_{i3}x_3\big), \quad \forall\mathbf{x}\in\kappa_\tau\big[\mathscr{B}^{\text{fluid}}\big]. \tag{36}$$

It can be shown that in our problem, the free surface of the fluid at the time instance $\boldsymbol{\tau}$ (marked as $\partial\mathbf{B}_{\tau,5}^{\text{fluid}}$ in Fig. 3a) is always part of a cylinder. More specifically, it can be shown that

$$\partial\mathbf{B}_{\tau,5}^{\text{fluid}} = \big\{\mathbf{x}\in\kappa_\tau\big[\mathscr{B}^{\text{fluid}}\big] \mid x_1^2 + x_2^2 = l_7^2\big\}. \tag{37}$$

The parameter l_7 in (37) is the distance of the center of $\partial\mathbf{B}_{\tau,5}^{\text{fluid}}$ from the rotation axis (see Fig. 3a).

The surface $\partial\mathbf{B}_{\tau,5}^{\text{fluid}}$ experiences the atmospheric pressure p^{atm} Pa, where $p^{\text{atm}} = 1.01325\times10^5$. Hence, one of the boundary conditions on $p_s^{\text{fluid}}[\cdot]$ is

$$p_s^{\text{fluid}}[\mathbf{x}] = p^{\text{atm}}, \quad \mathbf{x}\in\partial\mathbf{B}_{\tau,5}^{\text{fluid}}. \tag{38}$$

Solving (36) with the boundary condition (38), we get that

$$p_s^{\text{fluid}}[\mathbf{x}] = \frac{1}{2}\rho_0\omega_{\max}^2\big(x_1^2 + x_2^2 - l_7^2\big) + p^{\text{atm}}. \tag{39}$$

4.4 Material constitutive laws

4.4.1 Constitutive law for the spheroid

In (29) when $\mathbf{X}\in\kappa_R\big[\mathscr{B}^{\text{sprd}}\big]$

$$S_{ij}[\mathbf{X}] = \check{S}_{ij}^{\text{sprd}}[\mathbf{C}[\mathbf{X}]] - p_m^{\text{sprd}}[\mathbf{X}]J[\mathbf{C}[\mathbf{X}]](\mathbf{C}[\mathbf{X}])^{-1}, \tag{40a}$$

where $S_{ij}[\mathbf{X}]$ is the i-j^{th} component of $\boldsymbol{S}[\boldsymbol{X}]$, the 2$^{\text{nd}}$ Piola–Kirchhoff stress at the material particle $\boldsymbol{X}$,

$$J[\mathbf{C}] := \sqrt{\mathrm{Det}[\mathbf{C}]}, \tag{40b}$$

$\check{S}^{\text{sprd}}_{ij}[\cdot]$ is the i-j^{th} component of $\check{\mathbf{S}}^{\text{sprd}}[\cdot]$,

$$\check{\mathbf{S}}^{\text{sprd}}[\mathbf{C}] = \mu\,\text{Det}[\mathbf{C}]^{-\frac{1}{3}}\Big(\mathbf{I}_{3\times3} - \frac{1}{3}\text{Tr}[\mathbf{C}]\mathbf{C}^{-1}\Big), \tag{40c}$$

and μ Pa is the shear modulus. Here, $\text{Tr}[\cdot]$ is the trace operator. In (40a), the quantity $p^{\text{sprd}}_m[\mathbf{X}]$ acts as a Lagrange undetermined multiplier, which can be interpreted as the hydrostatic pressure at the material particle $\mathbf{X}$. Since $p^{\text{sprd}}_m[\cdot]$ is an unknown a priori, we solve (29) in conjunction with the incompressibility constraint

$$J[\mathbf{C}[\mathbf{X}]] = 1. \tag{41}$$

Equations (40) are the incompressible neo-Hookean material model from (Bonet and Wood 1997, equation 5.50).

4.4.2 Constitutive law for the 3D soft substrate

In (29) when $\mathbf{X} \in \kappa_{\text{R}}\big[\mathscr{B}^{\text{sub}}\big]$

$$S_{ij}[\mathbf{X}] = \check{S}^{\text{sub}}_{ij}[\mathbf{C}[\mathbf{X}]], \tag{42a}$$

where $\check{S}^{\text{sub}}_{ij}[\cdot]$ is the i-j^{th} component of $\check{\mathbf{S}}^{\text{sub}}[\cdot]$,

$$\begin{aligned}\check{\mathbf{S}}^{\text{sub}}[\mathbf{C}] = \mu\,\text{Det}[\mathbf{C}]^{-1/3}\Big(\mathbf{I}_{3\times3} - \frac{1}{3}\text{Tr}[\mathbf{C}]\mathbf{C}^{-1}\Big)\\ + \Big(\lambda + \frac{2}{3}\mu\Big)J[\mathbf{C}](J[\mathbf{C}]-1)\mathbf{C}^{-1}.\end{aligned} \tag{42b}$$

Here, λ Pa and μ Pa are the Lamé parameters. Equations (42) are the compressible neo-Hookean material model from (Bower 2009, Sect. 3.5.5).

4.5 Boundary conditions

The solution of (29) also requires the use of the following boundary conditions.

Let $\partial\mathbf{B}^{\text{sprd}}$ and $\partial\mathbf{B}^{\text{sub}}$ be the surfaces of the spheroid $\kappa_{\text{R}}\big[\mathscr{B}^{\text{sprd}}\big]$ and the substrate $\kappa_{\text{R}}\big[\mathscr{B}^{\text{sub}}\big]$, respectively. Let $\partial\mathbf{B}^{\text{sprd}}_{\text{cont}}$ and $\partial\mathbf{B}^{\text{sub}}_{\text{cont}}$ be the surfaces of $\kappa_{\text{R}}\big[\mathscr{B}^{\text{sprd}}\big]$ and $\kappa_{\text{R}}\big[\mathscr{B}^{\text{sub}}\big]$, respectively, that come into contact with each other (see Fig. 3b). They are both unknown a priori. The boundary conditions on $\partial\mathbf{B}^{\text{sprd}}_{\text{cont}}$ and $\partial\mathbf{B}^{\text{sub}}_{\text{cont}}$ are that there are no shear tractions on them, and the displacements of the spheroid and substrate on them, respectively, are such that

$$\bar{\mathbf{x}}^{\text{sprd}}\Big[\partial\mathbf{B}^{\text{sprd}}_{\text{cont}}\Big] = \bar{\mathbf{x}}^{\text{sub}}\Big[\partial\mathbf{B}^{\text{sub}}_{\text{cont}}\Big], \tag{43}$$

see Fig. 3a for an illustration.

Let $\partial\mathbf{B}^{\text{sub}}_1$ and $\partial\mathbf{B}^{\text{sub}}_2$ be the surfaces of $\kappa_{\text{R}}\big[\mathscr{B}^{\text{sub}}\big]$ shown in Fig. 3b. The boundary conditions on $\partial\mathbf{B}^{\text{sprd}} \setminus \partial\mathbf{B}^{\text{sprd}}_{\text{cont}}$ and $\partial\mathbf{B}^{\text{sub}} \setminus \partial\mathbf{B}^{\text{sub}}_{\text{cont}} \setminus \bigcup_{i=1}^{2}\partial\mathbf{B}^{\text{sub}}_i$ (see Fig. 3b), due to the spheroid's and substrate's, respective, interactions with the fluid media are

$$\big(\mathbf{C}[\mathbf{X}]\mathbf{S}[\mathbf{X}] - p^{\text{fluid}}_m[\mathbf{X}]\mathbf{I}_{3\times3}\big)\mathbf{N}[\mathbf{X}] = \mathbf{0}_{3\times1}, \tag{44a}$$

where $\mathbf{S}[\mathbf{X}] := \big(S_{ij}[\mathbf{X}]\big)_{i,j\in\mathscr{I}}$, $\mathbf{0}_{3\times1} \equiv (0,0,0)$, and $\mathbf{N}[\mathbf{X}]$ is the unit outward surface normal vector at the location $\mathbf{X}$ (see Fig. 3b for example). The field $p^{\text{fluid}}_m[\mathbf{X}]$ in (44a) is $p^{\text{fluid}}_s\big[\bar{\mathbf{x}}[\mathbf{X}]\big]$, where $p^{\text{fluid}}_s[\cdot]$ is given in (39). More concretely,

$$p^{\text{fluid}}_m[\mathbf{X}] = \frac{1}{2}\rho_0\omega^2_{\max}\Big(\big(X_1 + U^\star_1[\mathbf{X}]\big)^2 + \big(X_2 + U^\star_2[\mathbf{X}]\big)^2 - l_7^2\Big) + p^{\text{atm}}. \tag{44b}$$

We cannot independently calculate l_7 in our model. Therefore, in (44b), we approximate l_7 as L_7, the distance of the fluid's free surface to the rotation axis under the assumption that none of the continua (the spheroid, the fluid, and the substrate) deform (see Fig. 3b). Also, since $U^\star_1$, X_1, and $U^\star_2$ are much smaller than X_2, in (44b) we approximate $\big(X_1 + U^\star_1[\mathbf{X}]\big)$ as naught, and $\big(X_2 + U^\star_2[\mathbf{X}]\big)$ as X_2. In summary, we compute

$$p^{\text{fluid}}_m[\mathbf{X}] \approx \frac{1}{2}\rho_0\omega^2_{\max}\big(X_2^2 - L_7^2\big) + p^{\text{atm}}. \tag{44c}$$

An additional boundary condition on the substrate is that

$$U^\star_1[\mathbf{X}]X_1 = -U^\star_3[\mathbf{X}]X_3, \quad \forall\mathbf{X} \in \partial\mathbf{B}^{\text{sub}}_1, \tag{45a}$$

$$U^\star_2[\mathbf{X}] = 0, \quad \forall\mathbf{X} \in \partial\mathbf{B}^{\text{sub}}_2. \tag{45b}$$

The boundary condition (45a) is a consequence of setting the radial component of the displacement field on $\partial\mathbf{B}^{\text{sub}}_1$ (see Fig. 3b) to be naught, which we do to model the constraint from the enclosure (see Fig .1a). We choose the boundary condition (45b) to model the fact that the substrate sits in the enclosure (see Fig .1a), which constrains its deformation in the $\boldsymbol{E}_2$ direction on $\partial\mathbf{B}^{\text{sub}}_2$.

5 Coupled boundary value problems

As per our model, the motion of the spheroid and the 3D soft substrate is given by the family of deformation maps $\boldsymbol{x}_{\boldsymbol{\tau}}[\cdot]$. This family of deformation maps can be constructed using (10) once the displacement field components $U^\star_i[\cdot]$ are known. The restrictions of $U^\star_i[\cdot]$ to $\kappa_{\text{R}}\big[\mathscr{B}^{\text{sprd}}\big]$ (resp. $\kappa_{\text{R}}\big[\mathscr{B}^{\text{sub}}\big]$) are obtained by solving the partial differential equation (PDE) (29) over the region $\kappa_{\text{R}}\big[\mathscr{B}^{\text{sprd}}\big]$ (resp. $\kappa_{\text{R}}\big[\mathscr{B}^{\text{sub}}\big]$). We refer to the PDE (29) posed over the region $\kappa_{\text{R}}\big[\mathscr{B}^{\text{sprd}}\big]$ as the spheroid boundary value problem (BVP), and the PDE (29) posed over the region $\kappa_{\text{R}}\big[\mathscr{B}^{\text{sub}}\big]$ as the substrate BVP.

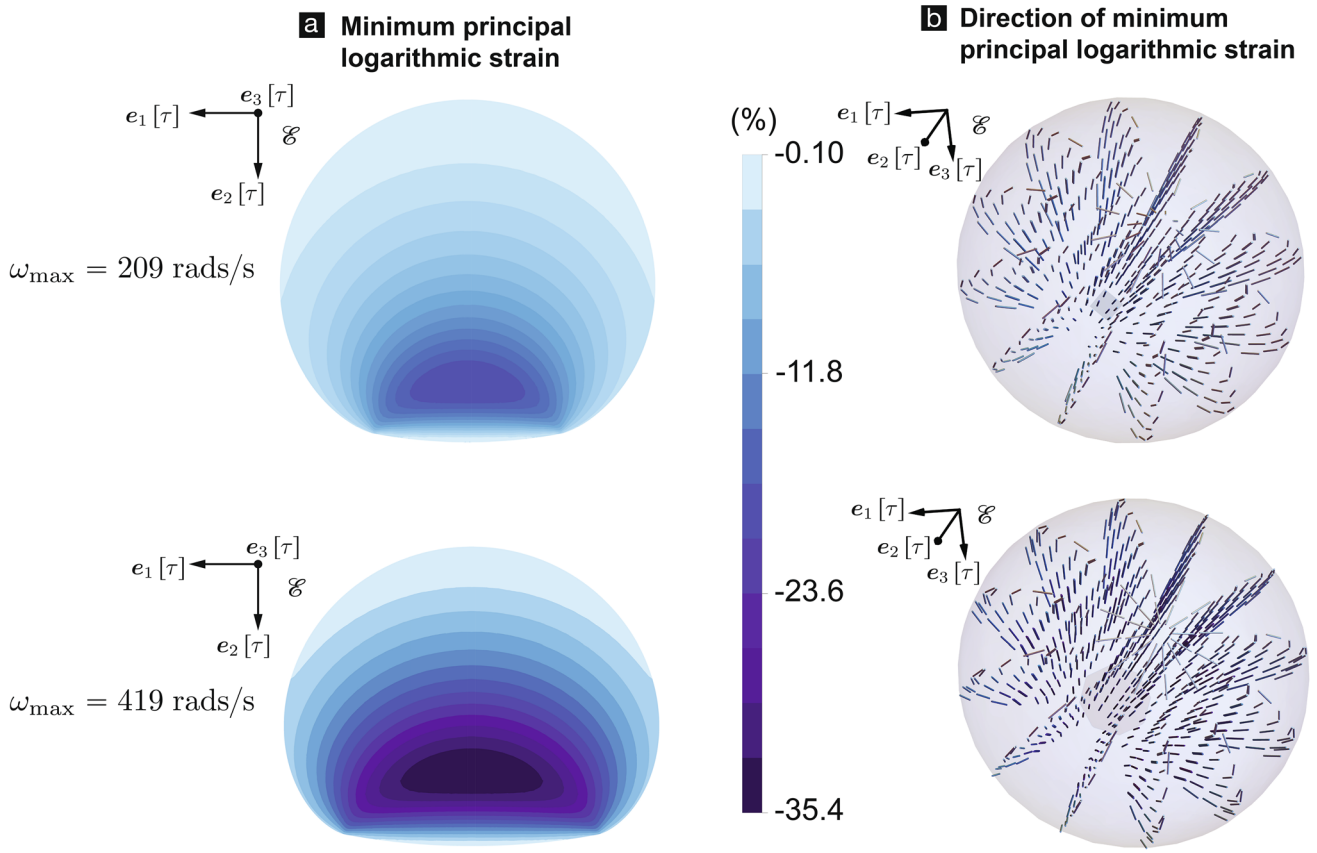

Fig. 4 Strains in the spheroid predicted by our theory for the representative values of angular velocity, geometry parameters, and material properties described in Sect. 6 at an arbitrary time instance τ. **a** Contour plots of the minimum principal value of the logarithmic strain tensor. The minimum principal value is the smallest eigenvalue. The logarithmic strain tensor is defined in Sect. 6.1. **b** Each line segment shows a section of the fiber associated with the eigenvectors that correspond to the minimum eigenvalue at the location of its midpoint

Recall that the functions $\{F_{im}S_{mj}\}[\cdot]$ appearing in (29) are defined as

$$\mathbf{X} \mapsto F_{im}[\mathbf{X}]S_{mj}[\mathbf{X}]. \tag{46}$$

In the spheroid (resp. substrate) BVP the $F_{im}[\cdot]$ in (46) are to be interpreted as the restrictions of the $F_{im}[\cdot]$ defined in (23b) to $\kappa_{\mathrm{R}}\left[\mathscr{B}^{\mathrm{sprd}}\right]$ (resp. $\kappa_{\mathrm{R}}\left[\mathscr{B}^{\mathrm{sub}}\right]$). For the spheroid (resp. substrate) BVP the $S_{mj}[\cdot]$ in (46) is given by the function (40) (resp. (42)). In the spheroid BVP, due to the presence of the Lagrange multiplier (pressure field) $p_m^{\mathrm{sprd}}[\cdot]$ in (40), the PDE (29) needs to be solved jointly with the incompressibility constraint equation (41). The boundary conditions in the spheroid and the substrate BVPs are detailed in Sect. 4.5.

Note that the contact boundary condition (43) is part of both the spheroid and the substrate BVPs. It couples the two BVPs, since it involves displacement components from both BVPs. Therefore, the two BVPs cannot be solved independently. We solve the spheroid and the substrate BVPs simultaneously using finite element techniques.

6 Representative numerical solutions of the theory

To get a preliminary understanding into the type of strains and stresses that the cortical spheroids experience in the constant angular velocity centrifuge-TBI-model, and for demonstrating our theory, we compute various strain and stress measures in the cortical spheroids using our theory for some representative values of angular velocity, geometry parameters, and material properties.

Typical lab grade centrifuges are capable of reaching top speeds in the range of 1000–5000 revolution per minute (RPM). Therefore, for the representative calculations, we consider angular velocities of 2000 RPM, i.e., 209 radians per second (rad/s); and 4000 RPM, i.e., 419 rad/s.

For the representative calculations, we take the 3D soft substrate to be composed of agarose hydrogel and the cortical spheroids and fluid media to be the ones described in (Dingle et al. 2015). Consequently, we take the densities of the 3D soft substrate, cortical spheroid, and fluid media to

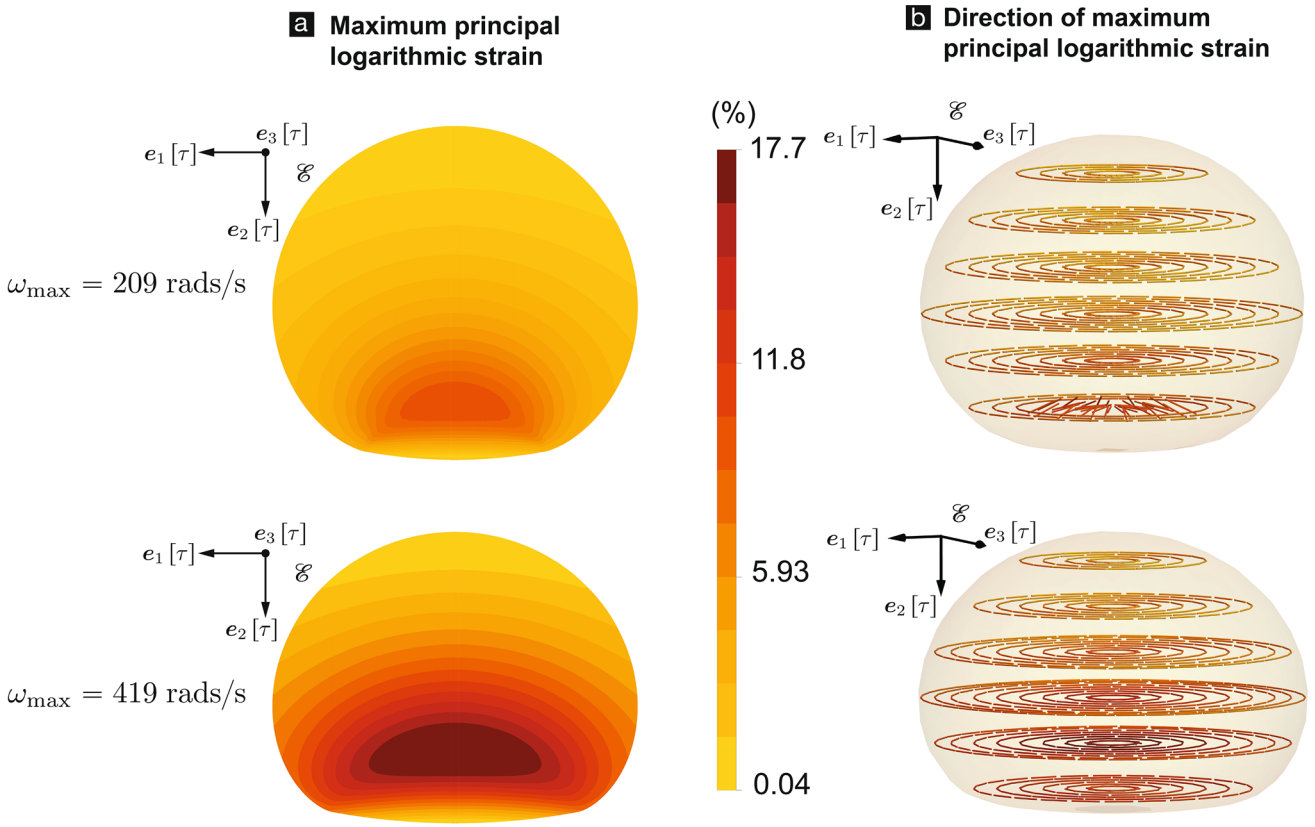

Fig. 5 Strains in the spheroid predicted by our theory for the representative values of angular velocity, geometry parameters, and material properties described in Sect. 6 at an arbitrary time instance τ. **a** Contour plots of the maximum principal value of the logarithmic strain tensor. The maximum principal value is the largest eigenvalue. The logarithmic strain tensor is defined in Sect. 6.1. **b** Each line segment shows a section of the fiber associated with the eigenvectors that correspond to the maximum eigenvalue at the location of its midpoint

be 1640, 1240, and 980 kg/m^3, respectively. Based on the measurements in (Mori et al. 2013; Normand et al. 2000), we take the agarose hydrogel's Lamé parameters to be $\lambda = 4.28571 \times 10^5$ Pa and $\mu = 1.07143 \times 10^5$ Pa. Based on the measurements in (Boulet et al. 2011), we take the shear modulus of the cortical spheroids to be $\mu = 1.33 \times 10^3$ Pa.

We take the values for the geometry parameters to be the ones given in Table 1.

Some strain measures from the representative calculations are shown in Figs. 4, 5 and 6 and stress measures in Figs. 7, 8, 9 and 10. The definitions of some of those strain (resp. stress) measures are discussed in Sect. 6.1 (resp. Sect. 6.2).

6.1 Strains

For the strain measure, we use the logarithmic strain tensor $\boldsymbol{H}_{\tau}[\boldsymbol{x}]$. The logarithmic strain tensor is defined as

$$\boldsymbol{H}_{\tau}[\boldsymbol{x}] = \ln \boldsymbol{V}_{\tau}[\boldsymbol{x}], \tag{47a}$$

where

$$\boldsymbol{V}_{\tau}[\boldsymbol{x}]\boldsymbol{V}_{\tau}[\boldsymbol{x}] := \boldsymbol{F}_{\tau}\left[\boldsymbol{x}_{\tau}^{-1}[\boldsymbol{x}]\right]\left(\boldsymbol{F}_{\tau}\left[\boldsymbol{x}_{\tau}^{-1}[\boldsymbol{x}]\right]\right)^{\mathsf{T}}. \tag{47b}$$

The co-rotational Cartesian components of $\boldsymbol{H}_{\tau}[\boldsymbol{x}]$ are defined as

$$H_{ij}[\mathbf{x}] = \boldsymbol{e}_i[\tau] \cdot \left\{\boldsymbol{H}_{\tau}[\check{\boldsymbol{x}}[\mathbf{x}, \tau]]\boldsymbol{e}_j[\tau]\right\}, \tag{48}$$

where $\check{\boldsymbol{x}}[\mathbf{x}, \tau]$ is the vector in $\mathbb{E}$ such that $\mathbf{x}$ is its set of co-rotational Cartesian co-ordinates at the time instance τ. We denote the matrix $\left(H_{ij}[\mathbf{x}]\right)_{i,j\in\mathscr{I}}$ as $\mathbf{H}^{\{\boldsymbol{e}_i[\tau]\}}[\mathbf{x}]$.

Let

$$\mathbf{H}^{\{c_i[\boldsymbol{x},\tau]\}}[\mathbf{x}] := \mathbf{R}[\mathbf{x}]\left\{\mathbf{H}^{\{\boldsymbol{e}_i[\tau]\}}[\mathbf{x}]\right\}\mathbf{R}[\mathbf{x}]^{\mathsf{T}}. \tag{49}$$

We call $\mathbf{H}^{\{c_i[\boldsymbol{x},\tau]\}}[\mathbf{x}]$, the co-rotational cylindrical components form of $\boldsymbol{H}_{\tau}[\boldsymbol{x}]$. We denote the (1, 1), (2, 2), (3, 3), and (1, 3) components of $\mathbf{H}^{\{c_i[\boldsymbol{x},\tau]\}}[\mathbf{x}]$, respectively, as $H_{rr}[\mathbf{x}]$, $H_{\theta\theta}[\mathbf{x}]$, $H_{zz}[\mathbf{x}]$, and $H_{rz}[\mathbf{x}]$.

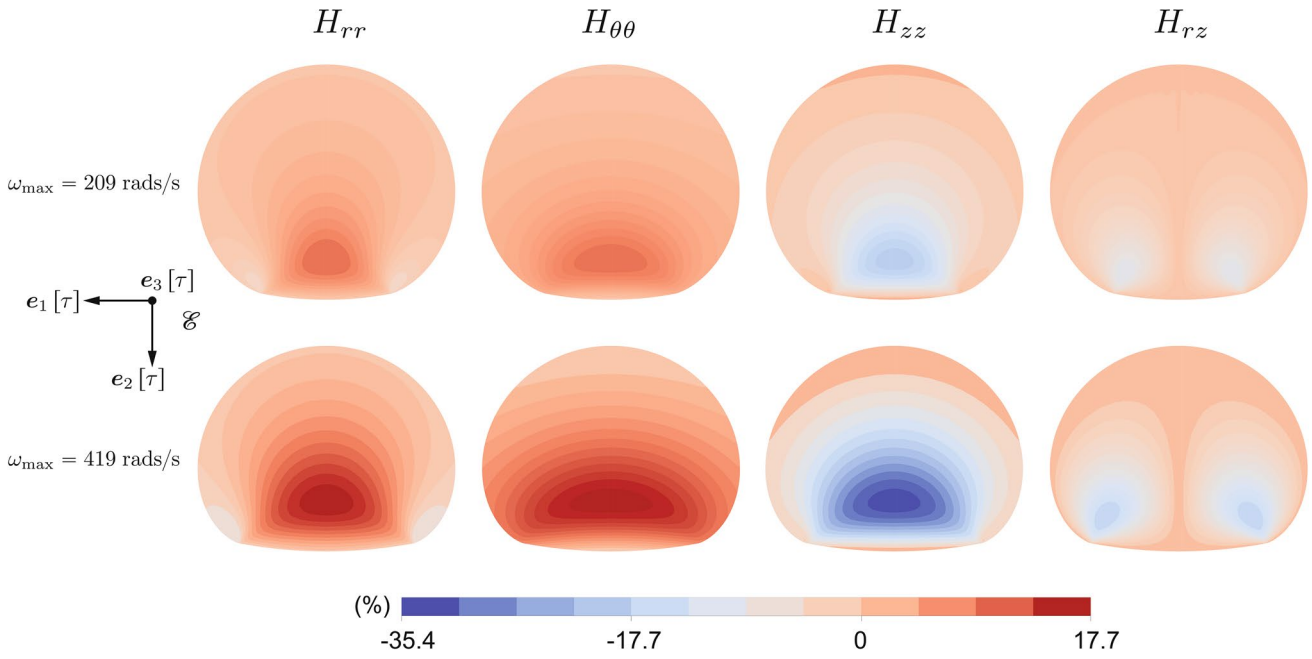

Fig. 6 Strains in the spheroid predicted by our theory for the representative values of angular velocity, geometry parameters, and material properties described in Sect. 6 at an arbitrary time instance τ. The logarithmic strain tensor is defined in Sect. 6.1. The columns show contour plots of H_{rr}, $H_{\theta\theta}$, H_{zz}, and H_{rz}, respectively, which are the co-rotational cylindrical components of the logarithmic strain tensor. They are defined in Sect. 6.1. The top row corresponds to the angular velocity 209 rad/s, and the bottom row to 419 rad/s

6.2 Stresses

For the stress measure, we use the Cauchy stress tensor. In Sect. 6.1 we defined the co-rotational Cartesian components of the logarithmic strain tensor, $\mathsf{H}^{\{\boldsymbol{e}_i[\tau]\}}[\mathbf{x}]$, using the logarithmic strain tensor, $\boldsymbol{H}_{\tau}[\boldsymbol{x}]$, and the co-rotational Cartesian basis $\big(\boldsymbol{e}_i[\tau]\big)_{i\in\mathscr{I}}$. In the same way, we can define the co-rotational Cartesian components of the Cauchy stress tensor, $\mathsf{T}^{\{\boldsymbol{e}_i[\tau]\}}[\mathbf{x}]$, using the Cauchy stress tensor, $\boldsymbol{T}_{\tau}[\boldsymbol{x}]$, and $\big(\boldsymbol{e}_i[\tau]\big)_{i\in\mathscr{I}}$. In Sect. 6.1, we further defined the co-rotational cylindrical components of the logarithmic strain tensor, $\mathsf{H}^{\{\boldsymbol{c}_i[\boldsymbol{x},\tau]\}}[\mathbf{x}]$, using $\mathsf{H}^{\{\boldsymbol{e}_i[\tau]\}}[\mathbf{x}]$ and the function $\mathsf{R}[\cdot]$ via (49). In the same way, we can define the the co-rotational cylindrical components of the Cauchy stress tensor, $\mathsf{T}^{\{\boldsymbol{c}_i[\boldsymbol{x},\tau]\}}[\mathbf{x}]$, using $\mathsf{T}^{\{\boldsymbol{e}_i[\tau]\}}[\mathbf{x}]$ and $\mathsf{R}[\cdot]$.

We denote the (1, 1), (2, 2), (3, 3), and (1, 3) components of $\mathsf{T}^{\{\boldsymbol{c}_i[\boldsymbol{x},\tau]\}}[\mathbf{x}]$, respectively, as $T_{rr}[\mathbf{x}]$, $T_{\theta\theta}[\mathbf{x}]$, $T_{zz}[\mathbf{x}]$, and $T_{rz}[\mathbf{x}]$.

The pressure at the location $\boldsymbol{x}$ at the time instance $\boldsymbol{\tau}$ is defined as negative one third the trace of $\boldsymbol{T}_{\tau}[\boldsymbol{x}]$.

7 Concluding remarks

1. In the proposed centrifuge-TBI-model design (Fig. 1), the cortical spheroids primarily undergo a type of squeezing deformation (Fig. 1c). However, with more sophisticated designs for the 3D soft substrate, it is possible to apply other types of deformations to the cortical spheroids.
2. We have stated earlier (see beginning of Sect. 2) that we restrict ourselves to the in vitro experiment in which the centrifuge's angular velocity is constant as a function of time. However, based on some preliminary experiments and noting that most micro-tissues are viscoelastic in nature, we believe that the final results from our theory will continue to apply with a minor modification even when the angular velocity is not a constant. Say the angular velocity changes with time as dictated by the function $\tau \mapsto \breve{\omega}_{\max}[\tau]$. Then, we believe that our results modified by replacing $\omega_{\max}$ in them with $\breve{\omega}_{\max}[\tau]$ will apply at the time instance τ. A caveat for our modified results to apply is that the variation of angular velocity with time be of a moderate character. That is, at the

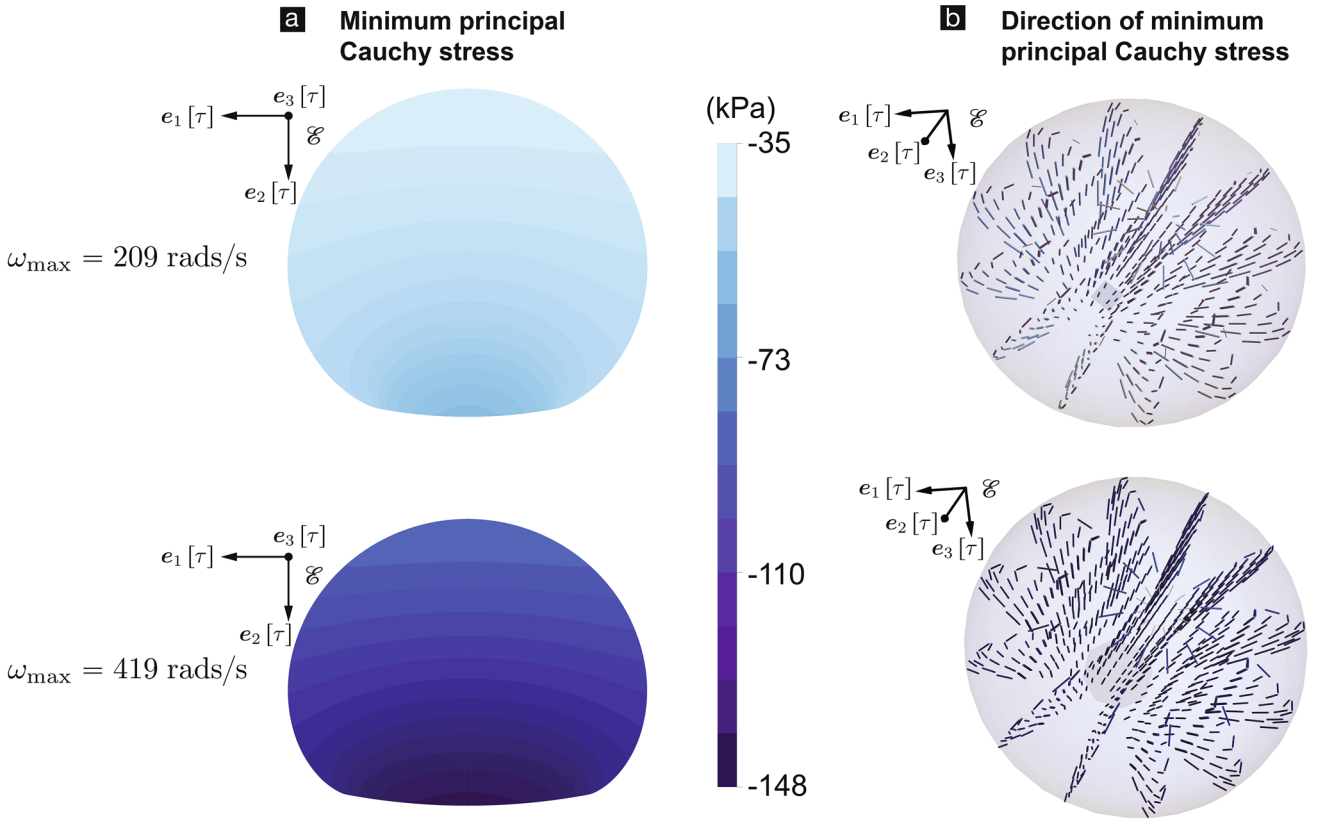

Fig. 7 Stresses in the spheroid predicted by our theory for the representative values of angular velocity, geometry parameters, and material properties described in Sect. 6 at an arbitrary time instance τ. **a** Contour plots of the minimum principal value of the Cauchy stress tensor. The minimum principal value is the smallest eigenvalue. **b** Each line segment shows a section of the fiber associated with the eigenvectors that correspond to the minimum eigenvalue at the location of its midpoint

least, the derivative of $\breve{\omega}[\cdot]$ be well defined and bounded. Since, clearly, our modified results will not apply when the angular velocity is changed abruptly, i.e., when $\breve{\omega}[\cdot]$ is a step function. (Such a step change in angular velocity will agitate the fluid media in addition to creating other complications.) Full 3D solution of the Navier–Stokes equations, in the context of the centrifuge-TBI-model, is needed in order to precisely determine the regime of applicability of our modified results.

3. The developed theory is fairly general. For deriving the numerical results shown in Figs. 4, 5, 6, 7, 8, 9 and 10, we modeled the mechanical behavior of the spheroids using the incompressible neo-Hookean constitutive law (40). This model does not incorporate any sophisticated material effects such as visco-elasticity, poro-elasticity, plasticity. We chose it not because we believe that the spheroid's deformation does not contain any such sophisticated effects, but rather because currently those effects are not sufficiently characterized in the spheroids, because of which (1) it is harder to justify the computational expense involved in incorporating those effects, and (2) the material constants in the material models incorporating those sophisticated effects will have to be selected in an almost arbitrary fashion. The elastic constants in the incompressible neo-Hookean constitutive law were chosen such that the spheroid's elastic behavior was consistent with the brain white matter's elasticity, which was characterized using magnetic resonance elastography (MRE) (Boulet et al. 2011), and the spheroids' contact deformations, which were characterized using an Atomic Force Microscope (Dingle et al. 2015). Once the more sophisticated material effects in the spheroid's mechanical deformation become well characterized, new numeri-

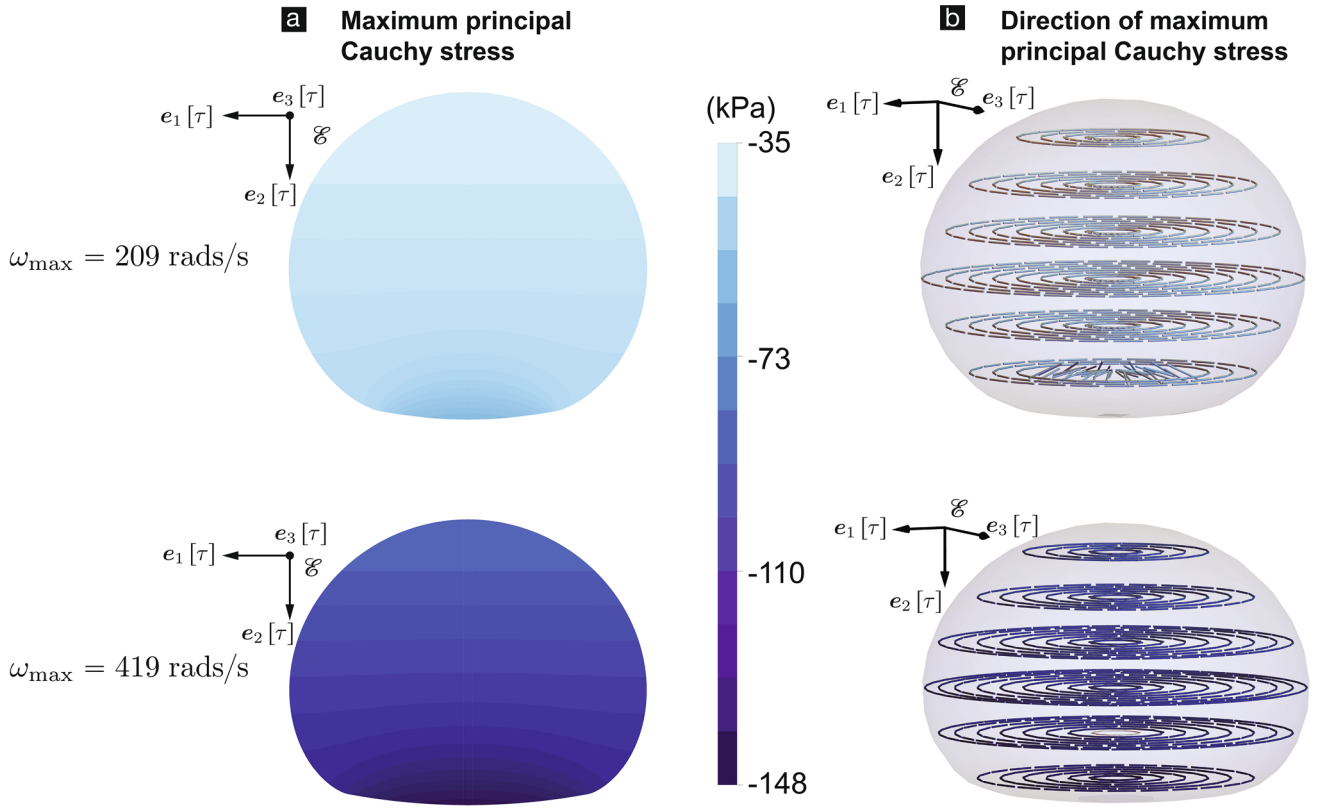

Fig. 8 Stresses in the spheroid predicted by our theory for the representative values of angular velocity, geometry parameters, and material properties described in Sect. 6 at an arbitrary time instance τ. **a** Contour plots of the maximum principal value of the Cauchy stress tensor. The maximum principal value is the largest eigenvalue. **b** Each line segment shows a section of the fiber associated with the eigenvectors that correspond to the maximum eigenvalue at the location of its midpoint

cal results can be derived in a straightforward manner from the developed theory by simply changing the spheroid's constitutive equation (40) to be something different that incorporates those effects. For example, it can be changed to the one developed in (Yuan et al. 2024), (Yuan et al. 2023), and (Yuan et al. 2022), which takes the brain's poro-elastic behavior into account.

4. There are several studies that focus on the deformation of a spherical elastic solid. A number of axi-symmetric solutions can be found in standard elasticity monographs and textbooks, such as (Love 2013) and (Barber 2002). For axi-symmetric solutions involving contact between two nominally spherical solids see, e.g., (Kesari and Lew 2011;Deng and Kesari 2019a, 2019b). For results involving both non-axi-symmetric deformation and contact see (Gutierrez et al. 2021). In the context of the vast amount of literature available on the deformation of a spherical elastic solid, a distinguishing aspect of the developed theory is that it contains the following four physical effects simultaneously: (a) contact between two deformable bodies, (b) finite deformation of both solids, (c) individual contact between the solids and a surrounding fluid, and (d) body forces on both solids and the fluid due to the rotation of their assembly.
5. From a mechanics and engineering perspective, we do not see anything that curtails one from using the idea of applying mechanical loads via centrifugation in other mechanobiology studies. Especially, in vitro traumatic injury studies can be envisioned with other micro-tissues, such as those composed of lung or liver cells.
6. As we mentioned in Sect. 1, the mechanical loading, i.e., the force on the cortical spheroid, can be easily and robustly tuned via the centrifuge's angular velocity and the volume of the fluid media. As we highlighted in Fig. 1c, the forces acting on the cortical spheroid consist of the tractions from the fluid media, tractions from the 3D soft substrate, and the body forces due to the rotations. The fact that the tractions on the cortical spheroid from the fluid media depend on the centrifuge's angular velocity and the volume of the fluid media can be seen from (44c).

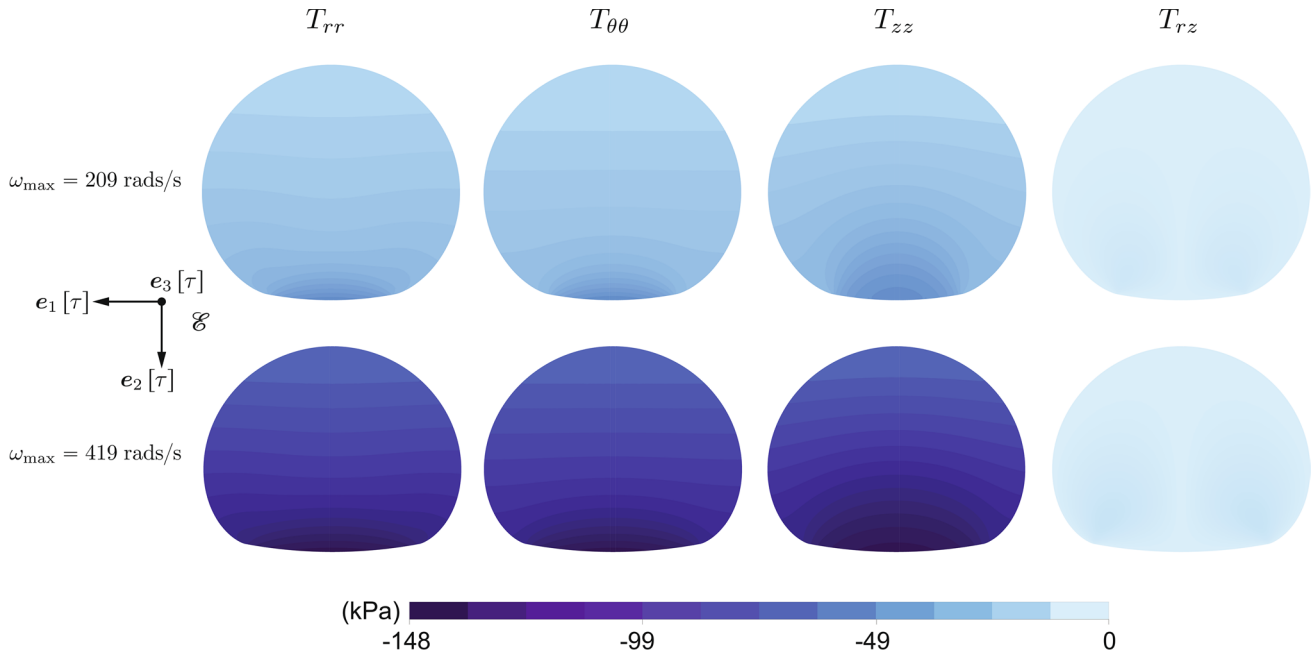

Fig. 9 Stresses in the spheroid predicted by our theory for the representative values of angular velocity, geometry parameters, and material properties described in Sect. 6 at an arbitrary time instance τ. The columns show contour plots of T_{rr}, $T_{\theta\theta}$, T_{zz}, and T_{rz}, respectively, which are the co-rotational cylindrical components of the Cauchy stress tensor (see Sect. 6.2 for details). The top row corresponds to the angular velocity 209 rad/s and the bottom row to 419 rad/s

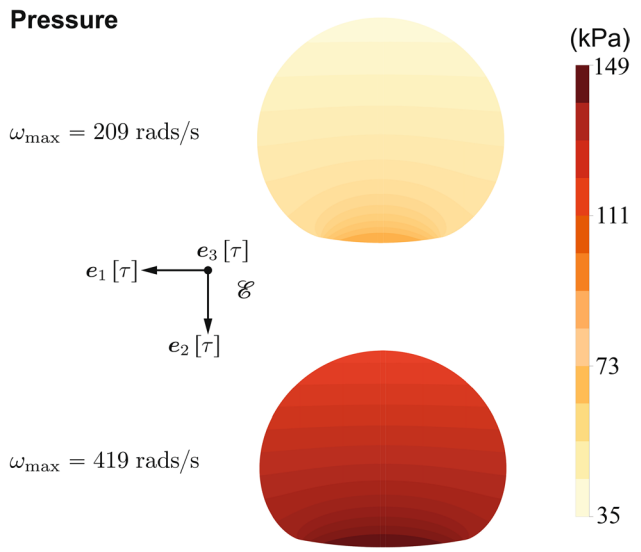

Fig. 10 Pressures in the spheroid predicted by our theory for the representative values of angular velocity, geometry parameters, and material properties described in Sect. 6 at an arbitrary time instance τ. The top plot corresponds to the angular velocity 209 rad/s, and the bottom plot to 419 rad/s

Appendix: Vanishing of the rate of deformation tensor

The rate of deformation tensor is defined as

$$\boldsymbol{D}_{\tau}[\boldsymbol{x}] = \frac{1}{2}\left(\boldsymbol{L}_{\tau}[\boldsymbol{x}] + \boldsymbol{L}_{\tau}[\boldsymbol{x}]^{\mathsf{T}}\right), \tag{50}$$

where $\boldsymbol{L}_{\tau}[\boldsymbol{x}]$ is the spatial velocity gradient, defined by

$$\boldsymbol{L}_{\tau}[\boldsymbol{x}] = \left\{\boldsymbol{\nabla}_{\boldsymbol{x}}\boldsymbol{v}_{\tau}\right\}[\boldsymbol{x}]. \tag{51}$$

From (18), (51) can be written as

$$\boldsymbol{L}_{\tau}[\boldsymbol{x}] = W_{ij}[\tau]\boldsymbol{v}_i[\tau] \otimes \boldsymbol{e}_j[\tau]. \tag{52}$$

From the definition of W_{ij} (15), it follows that $W_{ij} = -W_{ji}$. Then, from (52) and (50), we get that

$$\boldsymbol{D}_{\tau}[\boldsymbol{x}] = \boldsymbol{0}. \tag{53}$$

Acknowledgements The authors gratefully acknowledge support from the Panther Program and the Office of Naval Research (Dr. Timothy Bentley) under grant N000142112044.

Author contributions Y.W. carried out the research, discussed the results, and wrote the paper; R.D.G.C. discussed the results and wrote the paper; D.H.K. discussed the results and wrote the paper; H.K. designed the research, discussed the results, and wrote the paper.

Declarations

Competing interest The authors declare that they have no known competing financial interests or personal relationships that could have appeared to influence the work reported in this paper.

References

5810R Eppendorf. https://www.eppendorf.com/us-en

Barber JR (2002) Elasticity. Springer, USA

Bar-Kochba E, Scimone MT, Estrada JB, Franck C (2016) Strain and rate-dependent neuronal injury in a 3D *in vitro* compression model of traumatic brain injury. Sci Rep 6(1):30550

Bonet J, Wood RD (1997) Nonlinear continuum mechanics for finite element analysis. Cambridge University Press, Cambridge

Boulet T, Kelso ML, Othman SF (2011) Microscopic magnetic resonance elastography of traumatic brain injury model. J Neurosci Methods 201(2):296–306

Bower AF (2009) Applied mechanics of solids. CRC Press, USA

Carlsen RW, Fawzi AL, Wan Y, Kesari H, Franck C (2021) A quantitative relationship between rotational head kinematics and brain tissue strain from a 2-D parametric finite element analysis. Brain Multiphys 2:100024

Clark RS, Schiding JK, Kaczorowski SL, Marion DW, Kochanek PM (1994) Neutrophil accumulation after traumatic brain injury in rats: comparison of weight drop and controlled cortical impact models. J Neurotrauma 11(5):499–506

Deng W, Kesari H (2019) Depth-dependent hysteresis in adhesive elastic contacts at large surface roughness. Sci Rep 9(1):1639

Deng W, Kesari H (2019) Effect of machine stiffness on interpreting contact force-indentation depth curves in adhesive elastic contact experiments. J Mech Phys Solids 131:404–423

Dingle Y-TL, Boutin ME, Chirila AM, Livi LL, Labriola NR, Jakubek LM, Morgan JR, Darling EM, Kauer JA, Hoffman-Kim D (2015) Three-dimensional neural spheroid culture: an *in vitro* model for cortical studies. Tissue Eng Part C Methods 21(12):1274–1283

FDA (2021) Traumatic Brain Injury: What to Know About Symptoms, Diagnosis, and Treatment. https://www.fda.gov/consumers/consumer-updates/traumatic-brain-injury-what-know-about-symptoms-diagnosis-and-treatment

Feeney DM, Boyeson MG, Linn RT, Murray HM, Dail WG (1981) Responses to cortical injury: I. Methodology and local effects of contusions in the rat. Brain Res 211(1):67–77

Gurtin ME (1982) An introduction to continuum mechanics. Academic Press, USA

Gutierrez RA, Fang W, Kesari H, Darling EM (2021) Force sensors for measuring microenvironmental forces during mesenchymal condensation. Biomaterials 270:120684

Hanna ME, Pfister BJ (2023) Advancements in *in vitro* models of traumatic brain injury. Curr Opin Biomed Eng 25:100430

Kesari H, Lew AJ (2011) Effective macroscopic adhesive contact behavior induced by small surface roughness. J Mech Phys Solids 59(12):2488–2510

Liaudanskaya V, Chung JY, Mizzoni C, Rouleau N, Berk AN, Wu L, Turner JA, Georgakoudi I, Whalen MJ, Nieland TJ et al (2020) Modeling controlled cortical impact injury in 3D brain-like tissue cultures. Adv Healthcare Mater 9(12):2000122

Lin J-L, Huang Y-H, Shen Y-C, Huang H-C, Liu P-H (2010) Ascorbic acid prevents blood–brain barrier disruption and sensory deficit caused by sustained compression of primary somatosensory cortex. J Cerebral Blood Flow Metab 30(6):1121–1136

Love AEH (2013) A treatise on the mathematical theory of elasticity. Cambridge University Press, Cambridge

Maas A, Hukkelhoven C, Marshall L, Steyerberg E (2005) Prediction of outcome in traumatic brain injury with computed tomographic characteristics: a comparison between the computed tomographic classification and combinations of computed tomographic predictors. Neurosurgery 57(6):1173–1181

Maas AI, Menon DK, Manley GT, Abrams M, Åkerlund C, Andelic N, Aries M, Bashford T, Bell MJ, Bodien YG et al (2022) Traumatic brain injury: progress and challenges in prevention, clinical care, and research. Lancet Neurol 21(11):1004–1060

Masel BE, DeWitt DS (2010) Traumatic brain injury: a disease process, not an event. J Neurotrauma 27(8):1529–1540

McDonald BC, Saykin AJ, McAllister TW (2012) Functional MRI of mild traumatic brain injury (mTBI): progress and perspectives from the first decade of studies. Brain Imaging Behav 6:193–207

McIntosh T, Vink R, Noble L, Yamakami I, Fernyak S, Soares H, Faden A (1989) Traumatic brain injury in the rat: characterization of a lateral fluid-percussion model. Neuroscience 28(1):233–244

Mori Y, Kanazawa S, Watanabe M, Suenaga H, Okubo K, Nagata S, Fujihara Y, Takato T, Hoshi K (2013) Usefulness of agarose mold as a storage container for three-dimensional tissue-engineered cartilage. Mater Sci Appl 4:73–78

Murphy EJ, Horrrocks LA (1993) A model for compression trauma: pressure-induced injury in cell cultures. J Neurotrauma 10(4):431–444

Normand V, Lootens DL, Amici E, Plucknett KP, Aymard P (2000) New insight into agarose gel mechanical properties. Biomacromol 1(4):730–738

Rahaman MM, Fang W, Fawzi AL, Wan Y, Kesari H (2020) An accelerometer-only algorithm for determining the acceleration field of a rigid body, with application in studying the mechanics of mild traumatic brain injury. J Mech Phys Solids 143:104014

Shoemaker AR, Jones IE, Jeffris KD, Gabrielli G, Togliatti AG, Pichika R, Martin E, Kiskinis E, Franz CK, Finan JD (2021) Biofidelic dynamic compression of human cortical spheroids reproduces neurotrauma phenotypes. Disease Models Mech 14(12):048916

TBI Data | Concussion | Traumatic Brain Injury | CDC Injury Center. https://www.cdc.gov/traumaticbraininjury/data/index.html. Accessed: 21 July 2023

Teasdale G, Jennett B (1974) Assessment of coma and impaired consciousness: a practical scale. Lancet 304(7872):81–84

Wan Y, Fawzi AL, Kesari H (2022) Determining rigid body motion from accelerometer data through the square-root of a negative semi-definite tensor, with applications in mild traumatic brain injury. Comput Methods Appl Mech Eng 390:114271

Wan Y, Fang W, Carlsen RW, Kesari H (2023) A finite rotation, small strain 2D elastic head model, with applications in mild traumatic brain injury. J Mech Phys Solids 179:105362

Yuan T, Zhan W, Jamal A, Dini D (2022) On the microstructurally driven heterogeneous response of brain white matter to drug infusion pressure. Biomech Model Mechanobiol 21(4):1299–1316

Yuan T, Zhan W, Dini D (2023) Linking fluid-axons interactions to the macroscopic fluid transport properties of the brain. Acta Biomater 160:152–163

Yuan T, Shen L, Dini D (2024) Porosity-permeability tensor relationship of closely and randomly packed fibrous biomaterials and biological tissues: application to the brain white matter. Acta Biomater 173:123–134